# Repulsive Sema3E-Plexin-D1 signaling coordinates both axonal extension and steering via activating an autoregulatory factor, Mtss1

Namsuk Kim[1§], Yan Li[1§], Ri Yu[1], Anji Song[1], Hyo-Shin Kwon[1], Mi-Hee Jun[1], Jin-Young Jeong[1,2], Mi-Jin Kim[3], Jung-Woong Kim[3], and Won-Jong Oh[1*]

[1]Neurovascular Biology Laboratory, Neurovascular Unit Research Group, Korea Brain Research Institute, Daegu 41062, Republic of Korea

[2]Department of Brain and Cognitive Sciences, Daegu Gyeongbuk Institute of Science and Technology, Daegu 42988, Republic of Korea

[3]Department of Life Sciences, Chung-Ang University, Seoul 06974, Republic of Korea

[§]These authors contributed equally to this work.

*Corresponding author

E-mail: ohwj@kbri.re.kr (WJO)

# Abstract

In the developing nervous system, the axons of newly generated neurons extend toward destination targets following an exquisitely designed program. Axon guidance molecules are critical for neuronal pathfinding because they regulate both directionality and growth pace. However, little is known about the molecular mechanism that coordinates proper axonal extension and turning. Here, we show that Metastasis Suppressor 1 (Mtss1), a membrane protrusion protein, was a molecular facilitator ensuring axonal extension while sensitizing axons to Semaphorin 3E (Sema3E)-Plexin-D1 repulsive guidance cue. We demonstrate that Sema3E-Plexin-D1 signaling regulated Mtss1 expression in projecting striatonigral neurons. Mtss1 in turn induced Plexin-D1 localization to the growth cone where it signaled a repulsive cue to Sema3E. Moreover, Mtss1 was important for neurite extension independent of Sema3E. Ablation of Mtss1 expression reduced growth cone collapse and neurite extension in cultured neurons. *Mtss1*-knockout mice exhibited fewer striatonigral projections and irregular axonal routes, and these defects were recapitulated in *Plxnd1*-knockout mice. These findings demonstrate that repulsive axon guidance signaling activates an autoregulatory program to coordinate both axonal extension and steering during neuronal pathfinding.

**Keywords**: Axon guidance, Semaphorin3E, Plexin-D1, Mtss1, Basal ganglia development

# Introduction

In the developing nervous system, axons of newly generated neurons extend toward the destination targets and make connections to establish a functional circuit following an exquisitely designed program. In this long-range pathfinding process, axons encounter attractive and repulsiv3e signals from guidance molecules, and diverse combinations of ligand-receptor pairs communicate signals to a neuron from the environment (Kolodkin and Tessier-Lavigne, 2011; Tessier-Lavigne and Goodman, 1996). In addition to the conventional guidance mode, which has been established, recent studies have demonstrated signaling complexity through different mechanistic layers, such as crosstalk between guidance molecules (Dupin et al., 2015; Poliak et al., 2015), guidance switching between different holoreceptor complexes (Bellon et al., 2010) or guidance tuning by intrinsic regulators (Bai et al., 2011; Bonanomi et al., 2019). In general, the specific cognate guidance receptors that sense extracellular signals are mostly localized in growth cones, a specialized structure at the fore of a growing axon, and these receptors convey intracellular signaling cues within neurons (Dent et al., 2011; Franze, 2020). Therefore, proper signaling from guidance molecules in the growth cone surface is critical as axons travel to their destination. Because the axonal destination can be as far as a meter or more away from the soma, various transport systems consisting of specific adaptors and motor proteins transport guidance proteins to axon terminals and are thus critical for axonal movement (Dent et al., 2011; Winckler and Mellman, 2010). However, how individual guidance molecules are correctly delivered to growth cones and can accommodate the axonal growth pace is unclear, and the molecular machinery critical for the specific transportation of guidance molecules is unknown.

Growth cones are highly dynamic and motile cellular structures and facilitate axon growth and steering through activated receptors that alter cytoskeletal actin and microtubule assembly (Lowery and Vactor, 2009; Vitriol and Zheng, 2012). Therefore, guidance receptors undoubtedly need to be localized to these protrusive structures to control actin dynamics. Since actin filament assembly is mainly accompanied by membrane remodeling, a group of cytoskeletal scaffold proteins linking actin to the cell membrane must be activated (Vitriol and Zheng, 2012). One such protein group consists of Bin/Amphiphysin/Rvs (BAR) domain proteins, which have been implicated in many actin-associated membrane functions, such as cell motility, endocytosis, and organelle trafficking (Chen et al., 2013). Among these proteins, metastasis suppressor 1 (Mtss1, also called missing in metastasis), one of a few inverse BAR (I-BAR) domain subfamily proteins, is noticeable due to the capability of forming cellular

protrusions by promoting inverse membrane curvature (Machesky and Johnston, 2007). Because of its unique ability to connect the plasma membrane inner leaflet with actin, the role of Mtss1 has been characterized in promoting spine protrusions as well as neuronal dendrite growth (Galbraith et al., 2018; Saarikangas et al., 2015; Yu et al., 2016).

Semaphorin 3E, class-3 secreted semaphorin family protein, conveys guidance signals by directly binding with the Plexin-D1 receptor in both the nervous and vascular systems (Gu et al., 2005; Oh and Gu, 2013a). The Sema3E-Plexin-D1 pair mainly transmits a repulsive guidance cue via local cytoskeletal changes, thereby inhibiting axonal overgrowth and/or ectopic synapse formation in the central nervous system (Chauvet et al., 2007; Ding et al., 2012; Fukuhara et al., 2013; Mata et al., 2018; Pecho-Vrieseling et al., 2009). Previous studies have demonstrated that Sema3E-Plexin-D1 signaling is involved in dendritic synapse formation as well as traditional axon projection in basal ganglia circuitry, which is essential for diverse behavioral and cognitive functions in the brain (Ding et al., 2012; Ehrman et al., 2013). Notably, Plexin-D1 is expressed only in direct-pathway medium spiny neurons (MSN) projecting to the substantia nigra pars reticulata (SNr), one of two distinct types of MSNs in the striatum(Ding et al., 2012). Plexin-D1-positive striatonigral axons that travel through the corridor between the globus pallidus (GP) and reticular thalamic nucleus (rTh)/zona incerta (ZI), in which Sema3E molecules reside and emit repulsive signals to direct proper pathway formation toward the SNr (Chauvet et al., 2007; Ehrman et al., 2013). However, how the striatonigral pathway coordinates axonal growth and steering during pathfinding remains largely unknown.

In this study, we investigated the molecular mechanism of the repulsive Sema3E-Plexin-D1 guidance signaling pair in striatonigral-projecting neurons during mouse basal ganglia circuit development. We found that Sema3E-Plexin-D1 signaling coordinates axonal extension and diversion by enhancing the action of the facilitator protein Mtss1, during active striatonigral projection progression. In the context of the important and intricate networks in the brain, this study provides evidence showing that autoregulatory gene expression regulated by guidance signaling leads to the correct neuronal trajectory to the destination.

# Results

**Sema3E-Plexin-D1 signaling regulates Mtss1 expression in the developing striatum**

The majority of striatal neurons are MSNs, and the number of MSNs are equally divided into direct- and indirect-pathways (Surmeier et al., 2007). In a previous study, we found that *Plxnd1* is selectively expressed in direct-pathway MSNs (also called striatonigral neurons) projecting directly to the substantia nigra, with more than 45% of striatal neurons identified as Plexin-D1-positive neurons (Ding et al., 2012). Because of the relative abundance of Plexin-D1-positive neurons, we explored the potential downstream genes modulated by Sema3E-Plexin-D1 signaling. Specifically, we performed bulk RNA sequencing (RNA-seq) with striatal tissues at P5, when *Plxnd1* expression is high in the striatum, and compared the results obtained with control (*Plxnd1*$^{f/f}$) and conditional neuronal *Plxnd1*-knockout (*Nes-Cre;Plxnd1*$^{f/f}$) mice (Figure 1A). *Plxnd1* mRNA ablation in striatal tissues was validated in pan-neuronal *Plxnd1*-knockout (Nestin-Cre) mice (Figures S1A and S1B).

We also performed gene expression profile analysis, and the principal component analysis (PCA) plot showed that *Plxnd1* knockout accounted for the largest variance, and the results obtained in biological replicates showed high reproducibility (Figure S1C). Application of a conservative DEseq approach to RNA-seq data analysis confirmed 2,360 differentially expressed transcripts (Figure S1D). A Gene Ontology (GO) analysis was then performed, and biological connections between upregulated (1,240 transcripts) and downregulated (1,120 transcripts) differentially expressed genes (DEGs) in *Plxnd1*-knockout mice, compared to the expression of these genes in wild-type (control) mice, were identified (Figure S1E). Clustering of the downregulated DEGs in *Plxnd1*-knockout mice enabled their classification into several categories that were associated with axon guidance, regulation of dendritic spine morphology, and neuronal projection. Volcano plots present the statistical significance of differential transcript expression with respective fold change ($P < 0.05$, absolute log2 fold change (log2 FC) > 1) compared to the expression observed in the control group (Figure 1B).

Among the downregulated genes, *Mtss1* expression was particularly noticeable due to its high relevance to actin cytoskeletal rearrangement (Galbraith et al., 2018; Lin et al., 2005; Saarikangas et al., 2015). *Mtss1* gene expression was verified by qRT–PCR performed with *Plxnd1*-knockout cells (Figures S1F and S1G). The Mtss1 protein level was also markedly decreased in the knockout mice on P5 (Figures 1C and 1D). We also analyzed Mtss1 expression in *Sema3e*-knockout striatum samples obtained on P5 and found that its expression was decreased, but less dramatically than it was in *Plxnd1*-knockout striatum samples (Figures 1E and 1F). These

results suggested that Sema3E-Plexin-D1 signaling activation can increase Mtss1 expression at the transcriptional level in striatal neurons during development.

**Sema3E-Plexin-D1 signaling directly regulates Mtss1 expression in striatonigral-projecting neurons in a cell-autonomous manner**

Next, we analyzed the expression profiles of Plexin-D1 and Mtss1 from the development stage to the adult stage. Both Plexin-D1 and Mtss1 were expressed in the embryonic striatum, and their expression was highly elevated in the perinatal stage. Interestingly, Mtss1 expression was maintained at a relatively high level from E18.5 to P5 and then sharply declined and disappeared in the adult striatum, and although Plexin-D1 showed a similar expression pattern, its expression was maintained at a low level in the adult striatum (Figure 1G). To determine whether this Mtss1 expression is specific to Plexin-D1-positive neurons, we performed immunostaining with Drd1a-tdT mice, in which direct-pathway MSNs fluoresced red (Ade et al., 2011). As shown in Figure 1H, Mtss1 expression significantly overlapped with Drd1a-tdT striatal neurons (Figure S2), and its expression was reduced in *Plxnd1*-knockout mice, suggesting that Plexin-D1 signaling mediates Mtss1 expression in striatonigral projecting MSNs. Although Mtss1 was expressed at a low level regardless of Plexin-D1 presence on E16.5, it seemed to be under the control of Plexin-D1 signaling in the developing striatum from the last gestation period to the early postnatal period (Figures 1I and 1J). Furthermore, activating the Plexin-D1 receptor, the Sema3E ligand was predominantly expressed in the thalamus and released into the striatum, probably during thalamostriatal projection on E16.5, as had been observed in the early postnatal stage in a previous study (Figure S3) (Ding et al., 2012).

To determine whether Plexin-D1-driven Mtss1 expression is autonomously expressed in cells, we compared the Mtss1 level in cultured striatal neurons isolated from wild-type and *Plxnd1*-null mice. In the wild-type neurons, both Plexin-D1 and Mtss1 expression levels were low on day 3 *in vitro* (DIV3) and then had increased significantly by DIV6. In contrast, *Plxnd1*-knockout neurons failed to elevate Mtss1 expression by DIV6, suggesting that Mtss1 expression was induced in a cell-autonomous manner, not by indirect systemic changes at the circuitry level *in vivo* (Figures 1K and 1L).

**The Mtss1 I-BAR domain binds to Plexin-D1, and this interaction is Sema3E-independent**

Both Plexin-D1 and Mtss1 are localized on the cell membrane and regulate actin cytoskeletal rearrangement;

hence, we speculated that Plexin-D1 and Mtss1 may interact with each other to induce actin-related cellular events. To test whether Plexin-D1 and Mtss1 can physically interact, we generated multiple deletion constructs of human Plexin-D1 and Mtss1 (Figure 2A). When we overexpressed full-length Plexin-D1 and Mtss1 together in HEK293T cells, both proteins were successfully pulled down together (Figure 2B). However, Plexin-D1 with the intracellular domain (ICD) deleted failed to bind Mtss1, indicating direct intracellular Plexin-D1 and Mtss1 interaction (Figure 2C). When we overexpressed full-length Plexin-D1 and each Mtss1 deletion construct, every Mtss1 construct containing the I-BAR domain coprecipitated with Plexin-D1, but I-BAR-deficient Mtss1 failed to interact with Plexin-D1 (Figure 2D). In a previous study, Plexin-D1 was found to form a complex with SH3-domain binding protein 1 (SH3BP1), another BAR-domain family protein, and Sema3E binding to Plexin-D1 caused SH3BP1 release from the complex (Tata et al., 2014). Therefore, we examined whether Sema3E binding influences Mtss1 dissociation from Plexin-D1. In contrast to the effect on SH3BP1, Sema3E treatment did not interfere with Plexin-D1-Mtss1 complex formation, indicating that the complex is formed in a Sema3E-independent manner (Figure 2E).

**Mtss1 and Plexin-D1 form a complex and localize to F-actin-enriched protrusions of COS7 cells**

Because the Plexin-D1-Mtss1 complex is localized on the cell membrane, Mtss1 may regulate Plexin-D1 function at the cell surface. To investigate the role of Mtss1 on Plexin-D1 activity, we first examined whether Mtss1 affects the Plexin-D1 level on the plasma membrane by performing a surface molecule biotinylation analysis. We observed that overexpressed Plexin-D1 proteins in COS7 cells were efficiently biotinylated on the cell surface, but the Plexin-D1 protein level on the surface was not changed during Mtss1 coexpression (Figures 3A and 3B). Another potential mechanism by which Mtss1 may affect Plexin-D1 activity might be endocytic regulation because Plexin-D1 is rapidly endocytosed after Sema3E treatment (Burk et al., 2017). However, Mtss1 coexpression did not affect Sema3E-induced Plexin-D1 endocytosis (Figures S4A and S4B). Additionally, Mtss1 overexpression did not change the Sema3E binding affinity for Plexin-D1 (Figure S4C). These data suggest that Mtss1 does not affect Plexin-D1 cell surface distribution levels, endocytosis after Sema3E stimulation, or Sema3E binding to Plexin-D1.

Since Mtss1 plays a well-characterized role in regulating filopodia and spine precursors (Saarikangas et al., 2015; Yu et al., 2016), we hypothesized that Mtss1 forms a complex with Plexin-D1 that brings Plexin-D1 to filopodia-

like structures in COS7 cells. To test this possibility, we coexpressed Plexin-D1 and Mtss1 and analyzed their localization in COS7 cells. Mtss1 overexpression alone in COS7 cells led to a diverse degree of morphological changes, such as excessively spiked or thin and long protrusions. However, overexpression of the Mtss1 missing the I-BAR domain failed to generate these changes in protrusive shape (Figures S4D and S4E ). As shown in Figures 3C and 3D, when Plexin-D1 and Mtss1 were coexpressed, both proteins were highly colocalized in F-actin-enriched protrusions. However, overexpression of Plexin-D1 lacking the ICD colocalized with Mtss1 to a lesser degree than wild-type Plexin-D1, whereas Mtss1 was abundant in the protrusions. In addition, Mtss1 lacking the I-BAR domain, which possesses membrane-bending activity, did not generate filopodia-like protrusions in COS7 cells but was localized with -actin, including in marginal areas, probably via the Mtss1 WH2 domain (Mattila et al., 2003). Interestingly, although Plexin-D1 was evenly distributed throughout a cell, most Plexin-D1 was not present with Mtss1 missing the I-BAR domain. These results confirm that the Plexin-D1 and Mtss1 proteins form a complex in specialized cell structures such as filopodia.

**Mtss1 is colocalized with Plexin-D1 in the growth cone to potentiate repulsion**

To confirm that Mtss1 leads Plexin-D1 to protrusive structures, such as growth cones, in cultured neurons, Mtss1 and Plexin-D1 localization was analyzed by transfecting *Mtss1*-deficient striatal neurons with expression constructs carrying both proteins. Both overexpressed Plexin-D1 and Mtss1 proteins were transported to the growth cone and colocalized in F-actin-enriched regions (Figures 4A and 4B). However, the Mtss1 mutant lacking the I-BAR domain was expressed to a lesser degree in the growth cone than wild-type Mtss1 and failed to colocalize with Plexin-D1, which led to reduced Plexin-D1 localization in the growth cone (Figures 4A-4C). These results suggest that Mtss1 facilitates Plexin-D1 transport to the growth cone and that proper Plexin-D1 localization mediated through Mtss1 may contribute to triggering repulsive signaling by Plexin-D1 in response to Sema3E. To test this hypothesis, we performed a growth cone collapse assay on DIV3 in direct-pathway MSNs that had been genetically labeled with red fluorescence in Drd1a-tdT crossbred reporter mice. We found that wild-type Drd1a-tdT positive striatal neurons underwent a high collapse rate after exogenous Sema3E treatment, whereas the growth cones of neurons lacking *Mtss1* did not collapse at a significantly different rate (Figures 4D and 4E). Moreover, since *Mtss1* knockout did not alter the overall Plexin-D1 expression level in the neurons (Figures 4F and 4G), the reduced collapse rate in the *Mtss1*-deficient neurons was attributed to insufficient Plexin-

D1 transport to growth cones, not to reduced Plexin-D1 expression. In summary, Mtss1 targeting of Plexin-D1 to the growth cone is critical for robust Sem3E-induced repulsive signaling.

**Mtss1 is important for neurite extension in direct-pathway MSNs**

Previously, Sema3E-Plexin-D1 signaling was shown to act as a repulsive guidance cue that interferes with neurite growth in cultured MSNs (Chauvet et al., 2007). Consistent with this previous report, a reduction in neurite length of cultured direct-pathway MSNs on DIV3 in the presence of Sema3E was observed, whereas the length of the MSNs with *Plxnd1* knocked out was unaffected by Sema3E (Figures S5A and S5B). Next, to examine whether Mtss1 expression influences neurite growth by inducing proper Plexin-D1 localization, we cultured striatal neurons from wild-type or *Mtss1*-knockout mice for 3 days in the presence of exogenous Sema3E. As shown in Figures 4H and 4I, we observed growth retardation of the wild-type direct-pathway MSNs exposed to Sema3E, but neurons lacking *Mtss1* showed a significant reduction in neurite length regardless of Sema3E presence. Furthermore, we observed that a significant number of *Mtss1*-deficient neurons failed to extend neurites more than twice the cell body size (Figure S5C). Considering the reduced repulsive signaling response in the presence of Sema3E in the *Mtss1*-knockout cells due to the low level of Plexin-D1 at the axonal tip, increased neurite length was expected. However, because the neurite length of *Mtss1*-knockout cells was shorter than expected, we hypothesized that Mtss1 plays an important role in neurite extension to induce membrane protrusion. Lack of *Mtss1* in the cultured neurons presumably caused a severe neurite-growth-initiating defect, and the neuronal outgrowth defect had a greater effect than the increased growth potential caused by the weakened repulsive signal.

**The absence of Mtss1 reduces projection density as well as Plexin-D1 localization in the striatonigral pathway**

To investigate the role of Mtss1 in striatonigral pathway development, we performed an AP-Sema3E binding assay to examine the Plexin-D1-positive tract in brain tissue (Chauvet et al., 2007). In mice expressing wild-type *Mtss1* showed a significant level of Plexin-D1 in the neuronal pathway reaching the substantia nigra, whereas *Mtss1*-knockout mice exhibited poor neuronal projection and reduced Plexin-D1 localization on E17.5 (Figure 5A). In the coronal view, the bundle density of Plexin-D1-positive projections passing between the rTh and GP was reduced in the *Mtss1*-knockout mice (Figure 5B). Previously, *Sema3e* mutant embryos showed misrouting

defects in a few striatonigral projections (Chauvet et al., 2007), but we did not observe this phenotype, probably due to the dramatically reduced projections in the *Mtss1*-knockout brains. Because most mice with conditional Nestin-Cre-driven *Mtss1* deletion were born alive, we analyzed the Plexin-D1-positive striatonigral pathway at P0 and P5. Consistent with results obtained with E17.5 embryos (Figures 5C and 5D), *Mtss1*-deficient neonates showed fewer Plexin-D1-positive striatonigral projections in the coverage area and a reduced path width (Figures 5E-5I). Since no significant change in Plexin-D1 levels was observed in the striatum of *Mtss1*-deficient mice compared to those in littermate controls (Figures 5J and 5K), these results seemed to indicate that the weakening of the Plexin-D1-positive striatonigral pathway was caused by inappropriate Plexin-D1 distribution as well as neuronal projection impairment.

**The absence of Mtss1 reduces the axonal projection of direct-pathway MSNs, and the projections exhibit an irregular pattern**

To further identify Plexin-D1-positive striatonigral pathway defects, we crossed Drd1a-tdT transgenic reporter mice with conditional *Mtss1*-knockout mice and visualized the pathway in the offspring. Consistent with the results shown in Figure 5, the total boundary area with Drd1a-tdT-positive projections was smaller and less compact in the *Mtss1*-knockout mice than in the wild-type mice on P5 (Figures 6A-6C and 6L). On P30, the projection density defects were more obvious, but the boundary area in the wild-type and mutant mice was not significantly different, indicating that *Mtss1* deficiency led to the formation of fewer striatonigral axonal bundles (Figures 6D-6F and 6L). We assumed that Mtss1 regulates the initial striatonigral axonal projection during development of the neonate and that the pathway establishment ends by P7 (Morello et al., 2015); therefore, the scarcity of the projections may be clearer when the brain increases to the adult size. Through the sagittal view, we confirmed that the width of the striatonigral paths was narrower in the *Mtss1*-knockout neonates compared to that in the wild-type neonates, but any difference was not noticeable in adults (Figures 6G-6K). In another interesting observation, the descending striatonigral projections in the wild-type mice were relatively straight and untangled near the GP region. However, on P5, some *Mtss1* mutants showed irregular projection patterns with random directionality, but the misguidance defects were not apparent on P30 (Figures 6G and 6H, inset images), suggesting that low Plexin-D1 localization on the extending axons in the *Mtss1*-knockout mice may have weakened the proper guidance response.

Next, we wondered whether Mtss1 specifically contributes to descending striatonigral projection development or dendritic arborization. Since global *Mtss1* mutant mice had enlarged brain ventricles and decreased cortical thickness (Minkeviciene et al., 2019), we first examined whether *Mtss1* knockout causes any cellular impairment in the striatum. Using cleaved caspase 3 staining to detect apoptotic cells, we found few dying cells in the wild-type and *Mtss1* mutant neonates (Figures S6A and S6B), indicating no significant cell pathology induced by *Mtss1* expression deficiency. Because approximately 45% of striatal neurons are Mtss1-positive, we performed Golgi staining to observe dendritic defects, such as aberrant branching numbers and/or lengths, and found no difference between wild-type and *Mtss1* mutants on P5 (Figures S6C-S6E). Taken together, these results demonstrate that Sema3E-Plexin-D1-Mtss1 molecules are specifically involved in the proper guidance of descending striatonigral projections.

**_Plxnd1_ knockout recapitulates the striatonigral projection defects observed in the _Mtss1_ mutants**

Since Mtss1 expression is directly under the control of Sema3E-Plexin-D1 signaling, we investigated whether *Plxnd1* deletion leads to phenocopying of the striatonigral projection defects observed in *Mtss1*-knockout mice. During the neonatal period, the boundary area and compactness of descending striatonigral projections were small and loose, but only reduced projection density was observed in the *Plxnd1*-knockout mice, which was similar to that in the *Mtss1*-knockout mice, as shown in Figure 6 (Figures 7A-7F). We also observed irregular projection patterns near the GP similar to those seen in the *Mtss1*-knockout mice (Figures 7G and 7H). Previous studies have reported that Sema3E-Plexin-D1 signaling defects led to ectopic projection during development or misguidance in the striatonigral pathway of adults (Chauvet et al., 2007; Ehrman et al., 2013), but these phenotypes were not detected in our study. Collectively, our results confirm that Sema3E-Plexin-D1 signaling activates Mtss1 action, through which striatonigral neurons are extended and steered through the proper route to the target destination (Figure 7I).

# Discussion

Although many studies have reported the identification of proteins locally synthesized in the axon terminal (Jung et al., 2012), most proteins required for growth cone behavior are generated in and delivered from the soma. Because of the diverse roles of guidance molecules, such as driving neuronal cell migration, cell death, and axonal regeneration, as well as in traditional axonal navigation in the nervous system (Kolodkin and Tessier-Lavigne, 2011), guidance signaling is generally thought to be involved in the activation of a gene expression program in the nucleus. However, only a few studies have investigated gene or protein expression changes induced by guidance signaling at the transcriptional regulation level (Arvanitis et al., 2010; Yeh et al., 2014). Through a bulk RNA-seq analysis, we showed that Sema3E-Plexin-D1 signaling changed the expression of specific genes, including Mtss1, required for the precise axon guidance of striatonigral neurons. This finding was somewhat unexpected because it was counterintuitive: conventional repulsive guidance cues that mediate growth inhibition induce the upregulation of a positive regulator of neurite extension. We revealed that Mtss1 plays a dual role in axonal steering and extension. Therefore, our findings led to two important discoveries in understanding the axon guidance mechanism. First, axon guidance signaling can switch on the specific genetic program necessary for facilitating its own function, thereby generating the appropriate machinery to accomplish an intrinsic guidance role during neuronal pathfinding. Second, molecules such as Mtss1 coordinate negative and positive growth potentials in the axonal pathfinding route. Axon guidance cues require various auxiliary proteins to perform their programmed functions, in particular, transporting guidance receptors to the growth cone, endocytic sorting, and activating signaling cascades (O'Donnell et al., 2009), but none of the cofactors discovered to date have induced direct transcriptional regulation of the guidance signaling with which it is involved.

Our findings showed that the specific Mtss1 expression and axonal pathfinding process mediated through Sema3E-Plexin-D1 in striatal tissue were recapitulated in cultured neurons. These results imply that a cell-autonomous mechanism is involved in the guidance signaling that regulates Mtss1 expression and cellular behaviors. Although Sema3E-Plexin-D1 signaling regulated the expression of a set of genes in the present study, the precise signaling cascade that extends into the nucleus is still not completely understood. Increasing evidence has demonstrated that diverse extracellular stimuli induce dynamic changes in actin and microtubule cytoskeletal networks that depend on Rho family proteins, relaying signals that activate gene expression(Giehl et al., 2015;

Miralles et al., 2003; Percipalle and Visa, 2006; Samarakoon et al., 2010). Therefore, Plexin-D1 protein expression in the soma or dendrite during development may be involved in signaling related to the expression of other genes, and this signaling is probably mediated through actin cytoskeletal regulation.

Mtss1 promotes membrane curvature through the I-BAR domain and induces the redistribution of lipids in the membrane, thereby increasing the local phosphatidylinositol 4,5-bisphosphate ($PIP_2$) level at the negatively curved membrane. The elevation of local $PIP_2$ levels leads to membrane binding of the I-BAR domain via electrostatic interactions(Lin et al., 2018). Interestingly, Sema3E binding to Plexin-D1 elevated $PIP_2$ locally to activate Arf6, resulting in rapid focal adhesion disassembly(Sakurai et al., 2011). Since the Mtss1 I-BAR can interact with Plexin-D1 at the curved membrane (Figures 2 and 3), the local increase in $PIP_2$ in the curved membrane region may trigger signaling cascades. Although BAR-domain proteins play pivotal roles in membrane dynamics, a direct association between BAR-domain proteins and axon guidance receptors has not been extensively studied, and functional relevance *in vivo* is unclear. One example is the srGAP2 protein, which has been studied and shown to bind directly with the SH3 domain of the Robo1 guidance protein in cooperation with the F-BAR and RhoGAP domains(Guez-Haddad et al., 2015). Interestingly, in endothelial cells, Plexin-D1 forms a complex with SH3BP1, another small GTPase protein containing the F-BAR domain(Tata et al., 2014). Similar to the effect of Mtss1 and Plexin-D1 complex formation via the I-BAR domain, SH3BP1 colocalizes with Plexin-D1 at lamellipodia in a complex formed via the F-BAR domain and mediates Sema3E-induced cell collapse through Rac1 activity regulation. However, in contrast to the effect of the Mtss1 mutant missing the I-BAR domain, which failed to change the cell morphology, SH3BP1 lacking F-BAR led to cell collapse. Moreover, Sema3E binding to Plexin-D1 caused SH3BP1 to be released from the complex, whereas Sema3E did not interfere with the Plexin-D1-Mtss1 complex (Figure 2E). Because of the diverse roles played by Sema3E-Plexin-D1 across cell types, the effect of signaling induced by this complex may be determined by distinct downstream molecules that share structural similarities in a relevant biological context.

To modulate movement information conveyed through basal ganglia circuitry, two distinct types of striatal MSNs send axonal projections to different targets: a direct-pathway MSN expresses the dopamine D1 receptor to promote movement, and an indirect-pathway MSN expresses the dopamine D2 receptor to inhibit movement(Kreitzer and Malenka, 2008; Surmeier et al., 2007). Because of these unique functional and anatomical features, decoding the distinct molecular properties of the two types of MSNs and the regulatory mechanisms involved in circuitry

329 formation is important. A few previous transcriptome analyses have been performed with juvenile and adult mouse
330 brains(Heiman et al., 2008; Kronman et al., 2019; Lobo et al., 2006), but an understanding of the molecular
331 repertoire of each MSN during development is very limited. In the present study, Mtss1 was identified as a
332 selective molecule expressed in striatonigral projection neurons mediated by Sema3E-Plexin-D1 signaling, but its
333 expression is limited to only the early striatonigral projection period; therefore, the previous transcriptome
334 database in adults may have failed to identify Mtss1 as a specific marker molecule in direct-pathway MSNs.

335 In this study, Mtss1 expression was found to be relatively high during the perinatal period and then was
336 dramatically downregulated by P7 (Figure 1G), at which time striatonigral projection has ultimately been
337 completed(Morello et al., 2015). Consistent with a previous study showing that Plexin-D1-positive cells in the
338 striatum were first detected on E14.5(Zwaag et al., 2002), we found that its expression increased in the early
339 postnatal stage (Figure 1G). During a similar developing window in the striatonigral pathway, Sema3E was
340 predominantly expressed in the GP and rTh/ZI, which is located in the route to the substantia nigra; therefore, the
341 absence of repulsive Sema3E-Plexin-D1 signaling resulted in defects in striatonigral projection(Burk et al., 2017;
342 Chauvet et al., 2007; Ehrman et al., 2013). However, we did not find ectopic projections, misguidance defects, or
343 enlarged paths in *Mtss1*- or *Plxnd1*-knockout mice. However, we observed fewer projections with aberrantly
344 tangled patterns. These discrepancies may be explained by the following observations. First, because we used a
345 genetic model to selectively label the striatonigral projections, we could detect abnormal phenotypes at a better
346 specific resolution. Second, we noticed a certain degree of developmental retardation in the *Mtss1*- or *Plxnd1*-
347 knockout neonates, even among those in the same litter; therefore, we strictly selected samples on the basis of
348 body weight. However, despite the low striatonigral projection formation rate in the *Mtss1*- or *Plxnd1*-knockout
349 mice, the adult mice showed a normal overall range of projection boundary size and width, suggesting that a
350 decrease in repulsive signals in the mutants may have widened the descending projections. Third, the mouse
351 genetic background may have led to the observed phenotypic discrepancies. We previously observed that certain
352 vascular phenotypes were more evident in *Sema3e*-knockout mice with a 129SVE background than in those with
353 a C57BL/6 background(Oh and Gu, 2013b), implying that relatively minor defects may vary depending on the
354 genetic background.

355 Although there are simply two main views of the traditional axon guidance concept, attractive cue- and repulsive
356 cue-guided axon growth, axon terminals are constantly facing both types of signals *en route* to the destination. In

357 the present study, we showed that the repulsive guidance cues induced a dual-functioning facilitator through which
358 navigating axons ensure incessant extension to their target tissues while showing sensitivity and subsequent
359 steering in response to repulsive signals (Figure S7). Because of the tremendous wiring complexity in the central
360 nervous system, we expect that undiscovered molecules similar to those in the Sema3E-Plexin-D1-Mtss1 complex
361 are involved in the formation of other circuits.

# Materials and Methods

## Mice

*Plxnd1*$^{flox/flox}$ (*Plxnd1*$^{f/f}$) mice(Kim et al., 2011) and *Sema3e*$^{+/-}$ mice(Chauvet et al., 2007) were maintained on a C57BL/6 (#000664, The Jackson Laboratory) background. Nestin-Cre (#003771) and Drd1a-tdTomato (#016204) mice were obtained from The Jackson Laboratory (Bar Harbor, USA) and maintained on the same background. The frozen sperms of *Mtss1*$^{flox/+}$ mice were generously provided by Dr. Mineko Kengaku and rederived at the Laboratory Animal Resource Center in the Korea Research Institute of Bioscience and Biotechnology (Cheongju, Korea). All protocols for animal experiments were approved by the Institutional Animal Care and Use Committee of Korea Brain Research Institute (IACUC-18-00008, 20-00012). All experiments were performed according to the National Institutes of Health Guide for the Care and Use of Laboratory Animals and ARRIVE guidelines.

## Plasmids

A pBK-CMV vector containing VSV-tagged human Plexin-D1 cDNA(Gu et al., 2005) was recloned into a pCAG vector (pCAG-vsv-hPlexin-D1), and a Plexin-D1 construct lacking an intracellular domain (amino acids deleted: 1,299–1,925) was generated by PCR-based mutagenesis (pCAG-vsv-hPlexin-D1ΔICD). pAPtag-5-Sema3E vectors were reported previously(Chauvet et al., 2007), and the mouse Plexin-D1 extracellular domain (amino acids: 1–1,269) was amplified from mouse Plexin-D1 cDNA and directly cloned into a pAPtag-5 vector (pAPtag5-mPlexin-D1-ECD). The human full-length Mtss1 expression construct was purchased from Origene (pCMV6-hMtss1, Cat# RC218273, USA), and the following Myc-tagged Mtss1 deletion constructs (Mtss1ΔI-BAR [amino acids deleted: 1–250], Mtss1ΔWH2 [amino acids deleted: 714–745], and Mtss1-I-BAR [amino acids: 1–250]) were generated by PCR-based mutagenesis.

## RNA sequencing analysis

RNA sequencing (RNA-Seq) library preparation and sequencing were conducted at the ebiogen (Seoul, South Korea). Libraries were constructed using a NEBNext Ultra Directional RNA-Seq Kit customized with mouse-specific oligonucleotides for rRNA removal. Directional mRNA-Seq was conducted using the paired-end, 6 Gb read option of the Illumina HiSeq X10 system.

**Bioinformatic analysis for the RNA-Seq**

The entire analysis pipeline of RNA-Seq was coded using R software (ver. 3.6), which was controlled by systemPipeR (ver.1.18.2). Raw sequence reads were trimmed for adaptor sequences and masked for low-quality sequences using systemPipeR. Transcript quantification of RNA-Seq reads was performed with GenomicAlignments (ver.1.20.1) using reads aligned with the *Mus musculus* transcriptome annotation using Rsubread (ver. 1.24.6). The FPKM (Fragments Per Kilobase of transcript per Million mapped reads) values were calculated using the fpkm function of DESeq2 (ver. 1.24.0) and were processed using the robust median ratio method. Transcript reads were normalized by the voom function of Limma (ver. 3.40.6). To determine if a transcript was differentially expressed (DE), EdgeR (ver. 3.26.7) calculated the results based on the normalized counts from entire sequence alignments. Significantly DE transcripts with a fold change greater than the raw FPKM value (> 2) and adjusted p-value (< 0.01) in all experimental comparisons were selected and used for further analysis. Gene annotation was added by the online database using Ensembl biomaRt (ver. 2.40.4), and visualization was performed using the R base code and gplots package (ver. 3.0.1.1). For differentially expressed gene (DEG) sets, hierarchical cluster analysis was performed using complete linkage and Euclidean distance to measure similarity. All data analysis and the visualization of DEGs were conducted using R version 3.0.2 (www.r-project.org).

**Quantitative reverse transcription PCR (qRT-PCR)**

Total RNA was extracted from dissected tissue using TRIzol™ (15596026, Thermo). cDNA was synthesized from 200 ng of total RNA with a QuantiTect Reverse Transcription kit (205313, Qiagen). Quantitative PCR reactions were carried out in triplicate using SYBR Green I Master Mix (S-7563, Roche) on a LightCycler 480 system (Roche). Expression was calculated using the $2^{-\Delta\Delta Ct}$ method with *Gapdh* as a reference. The following primers were used (forward primer and reverse primer, respectively): *Mtss1*: 5'-CCTTTCCCTCATTGCCTGCCT, 5'-TCTGAGATGACGGGAACATGCC and *Gapdh*: 5'-TGACGTGCCGCCTGGAGAAAC, 5'-CCGGCATCGAAGG TGGAAGAG.

**Cell lines and primary striatal neuron culture**

COS7 or HEK293T cells were maintained at 37°C with 5% $CO_2$ in normal culture media (Dulbecco's modified Eagle's medium (DMEM, 11995-065, Gibco)) supplemented with 10% fetal bovine serum (FBS) and 1%

penicillin/streptomycin. Primary mouse striatal neurons were isolated from neonatal pups as described in a previous report with some modifications(Penrod et al., 2011). The whole striatum tissues including globus pallidus were digested with 20 units/ml of Papain (LS003124, Worthington, Lakewood USA) diluted in the dissection solution (5 mM of $MgCl_2$ and 5 mM of HEPES in 1×Hanks' Balanced Salt Solution, pH 7.2) followed by multiple washes in the inhibition solution (0.1% BSA and 0.1% Type II-O Trypsin inhibitor diluted in the dissection solution). The tissues were resuspended in neuronal plating media (1 mM pyruvic acid, 0.6% glucose, and 10% heat-inactivated horse serum in Minimum Essential Medium with Earle's Salts) and triturated fifty times with a fire-polished Pasteur pipette. The dissociated neurons were centrifuged at 1000 ×g for 5 min and resuspended with fresh neuronal plating media for cell counting. Then, cells were plated on coverslips or culture dishes coated with 50 μg/ml poly-D-lysine (P6407, Sigma) and 1 μg/ml laminin (354232, Corning) at a density of $3\times10^4$ cells/$cm^2$. After 4 h of incubation at 37°C, the plating media were replaced with neuronal growth media (0.5 mM L-Glutamine, B27 supplements in Neurobasal medium (10888022, Gibco)), and a quarter of the media was replaced with fresh growth media every 3 days until harvest.

**Transfection**

DNA expression constructs were transfected into the COS7 or HEK293T cells by Lipofectamine 2000 (11668019, Invitrogen) in OPTI-MEM (31985-070, Gibco) for 4 h according to the manufacturer's instructions, then replaced with normal culture media until the next procedure. For imaging analysis, 0.5 μg of DNA was transfected into COS7 cells ($1\times10^4$ cells/$cm^2$) cultured on coverslips in a 12-well plate. For biochemical analysis, 4 μg of DNA was transfected into HEK293T cells ($3\times10^4$ cells/$cm^2$) cultured on a 10-cm dish. To achieve high transfection efficiency into primary neurons, the nucleofection technique using a Lonza Amaxa Nucleofector was performed following the manufacturer's instructions (Basic Nucleofector Kit for Primary Mammalian Neuron, VAPI-1003). Four μg of expression constructs were added to at least $1\times10^6$ isolated neuronal cells for each electroporation, and the transfected cells were plated and cultured as described in the previous section.

**Alkaline phosphatase (AP)-conjugated ligand preparation and binding analysis**

AP-conjugated Sema3E and Plexin-D1-ECD ligands were generated in HEK293T cells, and ligand binding experiments were performed as described in previous reports(Chauvet et al., 2007, 2016). Briefly, the AP-conjugated expression construct was transfected into cells by Lipofectamine 2000 (11668019, Invitrogen) and

cultured overnight in DMEM containing 10% FBS. Then, the medium was replaced with OPTI-MEM and harvested at 5 days post-transfection. The collected conditioned medium was filtered to increase ligand concentration.

To measure the binding ability of AP-Sema3E to the Plexin-D1 receptor, COS7 cells on a six-well plate were transfected with each expression vector and cultured for 24 h. The next day, cells were washed in an HBHA buffer [1× HBSS, 0.5 mg/ml of BSA, 0.5% sodium azide, and 20 mM of HEPES (pH 7.0)] and incubated with 2 nM of AP or AP-Sema3E for 1 h at room temperature. After seven washes in the HBHA buffer, cells were lysed in 1% Triton X-100 and 10 mM of Tris-HCl (pH 8.0), and the supernatant was obtained by centrifugation at 13,000 ×g for 10 min. The lysates were heat-inactivated at 65°C for 10 min, and each lysate was used for AP concentration using a BioMate™ 3S spectrophotometer (Thermo Scientific) and the amount of protein was measured by BCA assay.

For AP-conjugated ligand binding analysis of tissues, 20-μm thick cryosections were fixed in cold methanol for 8 min and preincubated in 1×PBS containing 4 mM of $MgCl_2$ and 10% FBS for 1 h. Next, a binding solution (1×PBS–$MgCl_2$ and 20 mM of HEPES, pH 7.0) containing 2 nM of AP-Sema3E was applied, and sections were incubated for 2 h at room temperature. After five washes in 1×PBS–$MgCl_2$, sections were briefly soaked in acetone–formaldehyde fixative (60% acetone, 1.1% formaldehyde, and 20 mM of HEPES, pH 7.0) and heat-inactivated in 1×PBS at 65°C for 2 h. Next, sections were incubated in an AP buffer (NBT/BCIP tables, 11697471001, Roche) until clear purple precipitation was observed at room temperature. For quantification, three brain sections per animal were analyzed and averaged.

**Immunoblotting**

Brain tissue was collected in RIPA buffer with a protease inhibitor cocktail (11697498001, Roche), and protein amounts were quantified using a BCA protein assay kit (23227, Thermo Fisher Scientific). A total of 40 μg of protein was loaded into each well, after which it was separated on a sodium dodecyl sulfate (SDS) polyacrylamide gel and transferred to a polyvinylidene fluoride membrane (IPVH00010, Merck) at 100 V for 90 min. All membranes were blocked in Everyblot blocking buffer (12010020, Bio-Rad) for 1 h and probed overnight with primary antibodies in blocking buffer at 4°C. The primary antibodies included the following: anti-Mtss1 (1:1000, Novus, NBP2-24716), anti-Plexin-D1 (1:1000, AF4160, R&D Systems), anti-β-actin (1:5000, 5125S, Cell

Signaling), anti-Myc (1:1000, 2276S, Cell Signaling), anti-vsv (1:1000, ab3861, Abcam), and anti-Sema3E (1:500, LS-c353198, LSBio). The membranes were incubated in TBST, and the appropriate horseradish peroxidase (HRP)-conjugated secondary antibodies and bands were developed with enhanced chemiluminescence using Fusion FX7 (Vilber, Germany) and then analyzed using ImageJ software.

**Immunoprecipitation**

HEK293T cells were transfected with Lipofectamine 2000, and after 48 h they were lysed in a buffer consisting of 100 mM of Tris-HCl (pH 7.5), 100 mM of EDTA, 150 mM of NaCl, and 1% Triton X-100 with freshly added phosphate and protease inhibitors (11836170001, Roche). Cell lysates were centrifuged at 13,000 g for 10 min at 4°C, and supernatants were incubated with antibodies (1:200) at 4°C overnight. Then, protein lysates were incubated with a magnetic bead for 1 h at 4°C. Next, beads were washed five times with lysis buffer, and bound proteins were eluted with a 2×SDS sample buffer by heating the beads at 95°C for 5 min. Samples were then analyzed by SDS-PAGE and western blotting. The following antibodies were purchased from commercial sources: anti-Myc (1:1000, 2276S, Cell Signaling), anti-vsv (1:1000, ab3861, Abcam), anti-Mtss1 (1:1000, NBP2-24716, Novus), anti-Plexin-D1 (1:1000, AF4160, R&D Systems), and anti-β-Actin (1:5000, 5125S, Cell Signaling).

**Cell surface biotinylation and endocytosis analysis**

Transfected COS7 cells on a 100-mm dish were biotinylated by incubation in 1 mg/ml of NHS-SS-Biotin (21331, Thermo Scientific), diluted in 1×PBS containing 1 mM of $MgCl_2$ and 0.1 mM of $CaCl_2$ (PBS–MC) for 15 min, washed in PBS–MC containing 10 mM of glycine at least three times, and then rinsed in ice-cold PBS–MC twice at 4°C. For the negative control, cells were incubated in a stripping buffer (50 mM of glutathione, 75 mM of NaCl, 10 mM of EDTA, 75 mM of NaOH, and 1% bovine serum albumin (BSA)) and washed in PBS–MC twice. For the neutralization of glutathione, cells were incubated in PBS–MC containing 50 mM of iodoacetamide (I1149, Sigma) three times. All biotinylated or stripped cells were lysed in ice-cold RIPA buffer [50 mM of Tris-HCl (pH 8.0), 150 mM of NaCl, 1% NP-40, and 1% Sodium deoxycholate] with a protease inhibitor cocktail (11836170001, Roche), and 100 μg of protein extracts were incubated in pre-washed streptavidin agarose resin (20357, Thermo Scientific) overnight and rotated throughout. Cell extracts were serially washed in the bead-washing solution [Solution A: 150 mM of NaCl, 50 mM of Tris-HCl (pH 7.5), and 5 mM of EDTA; Solution B: 500 mM of NaCl, 50 mM of Tris-HCl (pH 7.5), and 5 mM of EDTA; Solution C: 500 mM of NaCl, 20 mM of Tris-HCl (pH 7.5),

and 0.2% BSA] followed by another wash in 10 mM of Tris-HCl (pH 7.5). The bound biotinylated proteins were recovered by adding a 2×sample buffer and boiling extracts for 5 min, and then the supernatants were applied to the western blot.

To analyze endocytic protein levels, cells were incubated for 25 min at 37°C in the presence of pre-warmed culture media with 2 nM of AP or AP-Sema3E ligands after surface biotinylation. Then, the biotinylated proteins remaining on the cell surface were removed by stripping procedures, and the rest of the experiment was continued as described in the above section. Excepting those used in the ligand stimulation process, all reagents were pre-chilled, and experiments were performed in an ice or cold chamber.

**Immunostaining**

For immunocytochemistry, cultured cells or neurons on coverslips were fixed in 4% paraformaldehyde (PFA) for 5 min and washed several times in PBS. Then, cells were permeabilized in PBST (PBS containing 0.1% Triton X-100) for 5 min, blocked with 5% horse serum in PBST for 60 min at room temperature, and incubated in primary antibodies diluted in the blocking solution overnight at 4°C. The next day, samples were washed with PBST three times and incubated for 1 h with Alexa Fluor 488-, 594-, or 647-conjugated-secondary antibodies (1:1000, Thermo). To enable visualization of the F-actins, Alexa Fluor-conjugated Phalloidin (1:50, Thermo) was added during the secondary antibody incubation. After being washed again with PBST, samples were mounted with Prolong Diamond antifade solution containing DAPI (P36962, Thermo). Image processing was performed using ImageJ or Adobe Photoshop (Adobe Photoshop CC2019) under identical settings. All other immunostaining procedures were the same as those described above. The following primary antibodies for immunocytochemistry were used: anti-vsv (1:1000, ab3861, Abcam), anti-Myc (1:1000, 2276S, Cell Signaling), Phalloidin Alexa Fluor 488 (1:50, A12379, Thermo), Phalloidin Alexa Fluor 647 (1:100, A22287, Thermo), anti-RFP (1:1000, ab62341, Abcam), anti-RFP (1:1000, MA5-15257, Thermo), and anti-alpha-tubulin (1:1000, T5168, Sigma). Images were collected using a Nikon Eclipse Ti-U microscope (Nikon, Japan), Leica TCS SP8 Confocal Microscope (Leica, Germany), or Structured Illumination Microscope (Nikon, Japan).

For immunohistochemistry with tissue samples, brains were fixed in 4% PFA overnight and equilibrated with 20% sucrose in 1×PBS. Mouse brain sections were cut into 20-μm slices on a cryostat (Leica Microsystems Inc., Buffalo Grove, IL, USA). Mouse brain sections were permeabilized in PBST (PBS containing 0.2% Triton X-100)

for 10 min, blocked with 2% BSA and 5% normal donkey serum in PBST for 60 min at room temperature, and then incubated in primary antibodies diluted with 2% BSA in PBST overnight at 4°C. The following primary antibodies were used: anti-Mtss1 (1:1000, NBP2-24716, Novus), anti-RFP (1:1000, MA5-15257, Thermo), and anti-cleaved caspase 3 (1:1000, 9661, Cell Signaling). After being washed with PBS/0.2% Tween 20 (PBST) three times, sections were incubated for 1 h with Alexa Fluor 488-, 594-, or 647-conjugated-secondary antibodies (1:1000, Invitrogen). For negative controls, brain sections were stained with secondary antibodies only. Image processing was performed using ImageJ or Adobe Photoshop (Adobe Photoshop CC2019).

**Growth cone collapse and neurite length analysis**

For growth cone collapse assay, striatal neurons at DIV 3 were incubated with 5 nM of AP or AP-Sema3E 3 for 25 min. For the preservation of the growth cone structure, 8% PFA was directly added to cultured neurons to equalize at 4% PFA for 10 min at 37°C, and subsequently, another 5-min round of 4% PFA fixation was performed on ice before the immunostaining procedure. Growth cone images were collected from tdT-positive neurons using a Structured Illumination Microscope (SIM, Nikon), and collapsed growth cones were determined blindly. Growth cones with broad lamellipodia were considered intact, whereas those with a few filopodia lacking lamellipodia were defined as collapsed according to previous guidelines(Oh and Gu, 2013b).

For measurement of the neurite length, dissociated striatal neurons were cultured for 3 days in the presence of 5-nM ligands and immunostained as described in the above section. The neurons were imaged by a fluorescence microscope (Nikon ECLIPSE Ti-U), and the longest neurite length from tdT-positive neurons was determined using ImageJ software. The neurites that formed a network with another neurite and those whose longest protrusions were smaller than twice the cell body diameter were excluded from measurement according to previous guidelines(Chauvet et al., 2016). For quantification of the degree of co-localization, Pearson's correlation coefficients were calculated using the manufacturer's software (Nikon, NIS-Elements software).

***In situ* hybridization (ISH)**

ISH was performed under RNase-free conditions as described in a previous study(Ding et al., 2012). After fixation in 4% PFA for 20 min, 20-μm thick cryosections sections were preincubated in a hybridization buffer (5× Denhardt's solution, 5× saline sodium citrate (SSC), 50% formamide, 0.25 mg/ml of Baker yeast tRNA, and 0.2 mg/ml of salmon sperm DNA) for 2 h at room temperature. Next, sections were hybridized in the same buffer

549 containing the indicated digoxigenin-conjugated riboprobe at 60°C overnight. After hybridization, sections were
550 washed in a serial SSC buffer and formamide solution and then preincubated in buffer 1 (100 mM Tris-HCl, pH
551 7.5, 150 mM NaCl) with a 1% blocking reagent (Roche) for 1 h at room temperature. Next, sections were
552 incubated with sheep anti-digoxigenin-alkaline phosphatase (AP) antibody (1:3000, Roche) for 90 min at room
553 temperature, washed in buffer 1, and then incubated in AP buffer (100 mM of Tris–HCl, pH 9.5; 100 mM of NaCl;
554 and 5 mM of $MgCl_2$) containing 4-nitro blue tetrazolium chloride (NBT, Roche), 5-bromo-4-chloro-3-indolyl-
555 phosphate (BCIP, Roche), and levamisole (1359302, Sigma) until purple precipitates were observed. After
556 mounting them with coverslips, the samples were analyzed using confocal laser-scanning microscopy with a
557 Nikon Eclipse Ti-U Microscope or Leica TCS SP8 Confocal Microscope. For double fluorescence ISH, the
558 tyramide signal amplification method with minor modification was used according to the manufacturer's
559 instructions (NEL753001KT, PerkinElmer). The following anti-sense riboprobes were used: *Plxnd1*(Ding et al.,
560 2012) and *Sema3e*(Gu et al., 2005).

561 **DiI injection**

562 For the tracing of the neural projection, small crystals of DiI (1.1-dioctadecyl-3,3,3,3-tetramethyl-
563 indocarbocyanine perchlorate, Sigma) were inserted into the thalamus of an E16.5 mouse brain fixed in 4% PFA
564 overnight and sealed with 2% agarose melt in 1×PBS. Then, the brain was incubated in 4% PFA at 37°C for 2
565 weeks and divided into 100-μm thick sections by vibratome (Leica VT200S). The serial brain slices were
566 immediately collected, and DiI-stained sections were imaged by a fluorescence microscope (Nikon Eclipse Ti-U).

567 **Striatonigral projection analysis**

568 For the analysis of striatonigral projections, P5 or P30 brains from wild-type (*Drd1a-tdT; Mtss1*$^{f/f}$), *Mtss1* cKO
569 (*Drd1a-tdT;Nes-cre;Mtss1*$^{f/f}$), or *Plxnd1* cKO (*Drd1a-tdT;Nes-cre;Plxnd1*$^{f/f}$) mice were fixed in 4% PFA overnight
570 and embedded in a 4% agarose block melt in PBS after being washed with PBS three times. Then, the areas of
571 interest in the brain were divided into 100-μm thick sections by a vibratome (Leica VT200S). The serial brain
572 slices were immediately collected and mounted with Prolong Diamond antifade solution containing DAPI
573 (P36962, Thermo). Sections were imaged by a fluorescence microscope (Nikon Eclipse Ti-U). To perform an
574 accurate phenotypic analysis including dendritic morphology described below, samples were chosen only from
575 the mutant littermates with ± 5% body weight variance.

576 **Golgi staining and dendrite analysis**

577 Golgi staining was conducted according to the manufacturer's protocol (FD Rapid GolgiStain kit (PK401A, FD
578 NeuroTechnologies, Inc.)). In brief, P5 mouse brains were immersed in a staining solution for 2 weeks before
579 being transferred to a wash solution for 4 days. 100-μm slices were obtained using a vibratome and collected on
580 gelatin-coated slides. During the staining process, slices were washed twice with distilled water for 4 min,
581 immersed in the staining solution for 10 min, and then washed again. Slices were then dehydrated, cleared in
582 xylene three times for 4 min, mounted with Eukitt® Quick-hardening mounting medium (Sigma, 03989), and
583 imaged by light microscopy. Image processing was performed using Neurolucida360 software.

584 **Statistical analysis**

585 The estimate of variance was determined by the standard error of the mean (SEM), and statistical significance
586 was set at $P<0.05$. All data were tested with Gaussian distribution using Shapiro-wilk test before statistical analysis.
587 Pairwise comparison was performed using the two-tailed Student's *t* test or Mann–Whitney test, and multiple
588 group analyses were conducted with one-way or two-way ANOVA with Tukey's or Bonferroni's multiple
589 comparisons test, or Kruskal-Wallis test with Dunn's multiple comparisons test. For growth cone collapse assay,
590 the $\chi 2$ test was used as previously reported(Burk et al., 2017). Statistical analyses were performed with Prism8
591 (GraphPad Software). At least three pairs of mice were used per experiment for all histological analyses. For the
592 quantification of image data, at least three brain sections per animal were collected and analyzed. All data analyses
593 were performed by an investigator blinded to the groups. No statistical methods were used to predetermine sample
594 sizes, but our sample sizes were similar to those generally employed in the field.

595 **Data and code availability**

596 The accession number for the RNA-Seq data reported in the present study is GSE196558.

## Acknowledgments

We thank Drs. Ayal Ben-Zvi, Soonmoon Yoo, and Chenghua Gu for reading the manuscript and providing critical advice; Dr. Chenghua Gu for providing *Sema3e* and *Plxnd1-flox* mice; Drs. Mineko Kengaku and Masayoshi Mishina for providing *Mtss1-flox* mouse; Juhyun Lee for helping with quantification; the Advanced Neural Imaging Center in KBRI for image analysis**.** This research was supported by the KBRI basic research program of the Korea Brain Research Institute funded by the Ministry of Science and ICT (KBRI 22-BR-01-02), the National Research Foundation (NRF) funded by the Korean government (NRF-2014R1A1A2058234), the Bio & Medical Technology Development Program of the NRF & funded by the Korean government (MSIT) (NRF-2020M3E5D9079766) to WO, and the Young Researcher Program of the National Research Foundation (NRF) funded by the Korean government (MSIT) (2020R1C1C1010509) to NK.

## Authors' contributions

WO conceived and designed the project. WO, NK, YL, RY, AS, HK, and JJ conducted experiments and acquired data. MK and JK performed RNA-seq and analyzed data. NK, JK, and WO wrote the manuscript.

**Declaration of interests:** The authors declare that they have no competing interests

# References

Ade, K.K., Wan, Y., Chen, M., Gloss, B., and Calakos, N. (2011). An Improved BAC Transgenic Fluorescent Reporter Line for Sensitive and Specific Identification of Striatonigral Medium Spiny Neurons. Frontiers Syst Neurosci *5*, 32.

Arvanitis, D.N., Jungas, T., Behar, A., and Davy, A. (2010). Ephrin-B1 Reverse Signaling Controls a Posttranscriptional Feedback Mechanism via miR-124. Mol Cell Biol *30*, 2508–2517.

Bai, G., Chivatakarn, O., Bonanomi, D., Lettieri, K., Franco, L., Xia, C., Stein, E., Ma, L., Lewcock, J.W., and Pfaff, S.L. (2011). Presenilin-Dependent Receptor Processing Is Required for Axon Guidance. Cell *144*, 106–118.

Bellon, A., Luchino, J., Haigh, K., Rougon, G., Haigh, J., Chauvet, S., and Mann, F. (2010). VEGFR2 (KDR/Flk1) Signaling Mediates Axon Growth in Response to Semaphorin 3E in the Developing Brain. Neuron *66*, 205–219.

Bonanomi, D., Valenza, F., Chivatakarn, O., Sternfeld, M.J., Driscoll, S.P., Aslanian, A., Lettieri, K., Gullo, M., Badaloni, A., Lewcock, J.W., et al. (2019). p190RhoGAP Filters Competing Signals to Resolve Axon Guidance Conflicts. Neuron *102*, 602-620.e9.

Burk, K., Mire, E., Bellon, A., Hocine, M., Guillot, J., Moraes, F., Yoshida, Y., Simons, M., Chauvet, S., and Mann, F. (2017). Post-endocytic sorting of Plexin-D1 controls signal transduction and development of axonal and vascular circuits. Nat Commun *8*, 14508.

Chauvet, S., Cohen, S., Yoshida, Y., Fekrane, L., Livet, J., Gayet, O., Segu, L., Buhot, M.-C., Jessell, T.M., Henderson, C.E., et al. (2007). Gating of Sema3E/PlexinD1 Signaling by Neuropilin-1 Switches Axonal Repulsion to Attraction during Brain Development. Neuron *56*, 807–822.

Chauvet, S., Mire, E., and Mann, F. (2016). Semaphorin Signaling, Methods and Protocols. Methods Mol Biology *1493*, 223–235.

Chen, Y., Aardema, J., and Corey, S.J. (2013). Biochemical and functional significance of F-BAR domain proteins interaction with WASP/N-WASP. Semin Cell Dev Biol *24*, 280–286.

Dent, E.W., Gupton, S.L., and Gertler, F.B. (2011). The Growth Cone Cytoskeleton in Axon Outgrowth and Guidance. Csh Perspect Biol *3*, a001800.

Ding, J.B., Oh, W.-J., Sabatini, B.L., and Gu, C. (2012). Semaphorin 3E–Plexin-D1 signaling controls pathway-specific synapse formation in the striatum. Nat Neurosci *15*, 215–223.

Dupin, I., Lokmane, L., Dahan, M., Garel, S., and Studer, V. (2015). Subrepellent doses of Slit1 promote Netrin-1 chemotactic responses in subsets of axons. Neural Dev *10*, 5.

Ehrman, L.A., Mu, X., Waclaw, R.R., Yoshida, Y., Vorhees, C.V., Klein, W.H., and Campbell, K. (2013). The LIM homeobox gene Isl1 is required for the correct development of the striatonigral pathway in the mouse. Proc National Acad Sci *110*, E4026–E4035.

Franze, K. (2020). Integrating Chemistry and Mechanics: The Forces Driving Axon Growth. Annu Rev Cell Dev Bi *36*, 1–23.

650 Fukuhara, K., Imai, F., Ladle, D.R., Katayama, K., Leslie, J.R., Arber, S., Jessell, T.M., and Yoshida, Y. (2013).
651 Specificity of Monosynaptic Sensory-Motor Connections Imposed by Repellent Sema3E-PlexinD1 Signaling.
652 Cell Reports *5*, 748–758.

653 Galbraith, K.K., Fujishima, K., Mizuno, H., Lee, S.-J., Uemura, T., Sakimura, K., Mishina, M., Watanabe, N.,
654 and Kengaku, M. (2018). MTSS1 Regulation of Actin-Nucleating Formin DAAM1 in Dendritic Filopodia
655 Determines Final Dendritic Configuration of Purkinje Cells. Cell Reports *24*, 95-106.e9.

656 Giehl, K., Keller, C., Muehlich, S., and Goppelt-Struebe, M. (2015). Actin-Mediated Gene Expression Depends
657 on RhoA and Rac1 Signaling in Proximal Tubular Epithelial Cells. Plos One *10*, e0121589.

658 Gu, C., Yoshida, Y., Livet, J., Reimert, D.V., Mann, F., Merte, J., Henderson, C.E., Jessell, T.M., Kolodkin,
659 A.L., and Ginty, D.D. (2005). Semaphorin 3E and Plexin-D1 Control Vascular Pattern Independently of
660 Neuropilins. Science *307*, 265–268.

661 Guez-Haddad, J., Sporny, M., Sasson, Y., Gevorkyan-Airapetov, L., Lahav-Mankovski, N., Margulies, D.,
662 Radzimanowski, J., and Opatowsky, Y. (2015). The Neuronal Migration Factor srGAP2 Achieves Specificity in
663 Ligand Binding through a Two-Component Molecular Mechanism. Structure *23*, 1989–2000.

664 Heiman, M., Schaefer, A., Gong, S., Peterson, J.D., Day, M., Ramsey, K.E., Suárez-Fariñas, M., Schwarz, C.,
665 Stephan, D.A., Surmeier, D.J., et al. (2008). A Translational Profiling Approach for the Molecular
666 Characterization of CNS Cell Types. Cell *135*, 738–748.

667 Jung, H., Yoon, B.C., and Holt, C.E. (2012). Axonal mRNA localization and local protein synthesis in nervous
668 system assembly, maintenance and repair. Nat Rev Neurosci *13*, 308–324.

669 Kim, J., Oh, W.-J., Gaiano, N., Yoshida, Y., and Gu, C. (2011). Semaphorin 3E–Plexin-D1 signaling regulates
670 VEGF function in developmental angiogenesis via a feedback mechanism. Gene Dev *25*, 1399–1411.

671 Kolodkin, A.L., and Tessier-Lavigne, M. (2011). Mechanisms and Molecules of Neuronal Wiring: A Primer.
672 Csh Perspect Biol *3*, a001727.

673 Kreitzer, A.C., and Malenka, R.C. (2008). Striatal Plasticity and Basal Ganglia Circuit Function. Neuron *60*,
674 543–554.

675 Kronman, H., Richter, F., Labonté, B., Chandra, R., Zhao, S., Hoffman, G., Lobo, M.K., Schadt, E.E., and
676 Nestler, E.J. (2019). Biology and Bias in Cell Type-Specific RNAseq of Nucleus Accumbens Medium Spiny
677 Neurons. Sci Rep *9*, 8350.

678 Lin, J., Liu, J., Wang, Y., Zhu, J., Zhou, K., Smith, N., and Zhan, X. (2005). Differential regulation of cortactin
679 and N-WASP-mediated actin polymerization by missing in metastasis (MIM) protein. Oncogene *24*, 2059–
680 2066.

681 Lin, X., Wang, H., Lou, Z., Cao, M., Zhang, Z., and Gu, N. (2018). Roles of PIP2 in the membrane binding of
682 MIM I-BAR: insights from molecular dynamics simulations. Febs Lett *592*, 2533–2542.

683 Lobo, M.K., Karsten, S.L., Gray, M., Geschwind, D.H., and Yang, X.W. (2006). FACS-array profiling of
684 striatal projection neuron subtypes in juvenile and adult mouse brains. Nat Neurosci *9*, 443–452.

685 Lowery, L.A., and Vactor, D.V. (2009). The trip of the tip: understanding the growth cone machinery. Nat Rev
686 Mol Cell Bio *10*, 332–343.

687 Machesky, L.M., and Johnston, S.A. (2007). MIM: a multifunctional scaffold protein. J Mol Med *85*, 569–576.

Mata, A., Gil, V., Pérez-Clausell, J., Dasilva, M., González-Calixto, M.C., Soriano, E., García-Verdugo, J.M., Sanchez-Vives, M.V., and Río, J.A. del (2018). New functions of Semaphorin 3E and its receptor PlexinD1 during developing and adult hippocampal formation. Sci Rep *8*, 1381.

Mattila, P.K., Salminen, M., Yamashiro, T., and Lappalainen, P. (2003). Mouse MIM, a Tissue-specific Regulator of Cytoskeletal Dynamics, Interacts with ATP-Actin Monomers through Its C-terminal WH2 Domain*. J Biol Chem *278*, 8452–8459.

Minkeviciene, R., Hlushchenko, I., Virenque, A., Lahti, L., Khanal, P., Rauramaa, T., Koistinen, A., Leinonen, V., Noe, F.M., and Hotulainen, P. (2019). MIM-Deficient Mice Exhibit Anatomical Changes in Dendritic Spines, Cortex Volume and Brain Ventricles, and Functional Changes in Motor Coordination and Learning. Front Mol Neurosci *12*, 276.

Miralles, F., Posern, G., Zaromytidou, A.-I., and Treisman, R. (2003). Actin Dynamics Control SRF Activity by Regulation of Its Coactivator MAL. Cell *113*, 329–342.

Morello, F., Prasad, A.A., Rehberg, K., Sá, R.V. de, Antón-Bolaños, N., Leyva-Diaz, E., Adolfs, Y., Tissir, F., López-Bendito, G., and Pasterkamp, R.J. (2015). Frizzled3 Controls Axonal Polarity and Intermediate Target Entry during Striatal Pathway Development. J Neurosci *35*, 14205–14219.

O'Donnell, M., Chance, R.K., and Bashaw, G.J. (2009). Axon Growth and Guidance: Receptor Regulation and Signal Transduction. Annu Rev Neurosci *32*, 383–412.

Oh, W.-J., and Gu, C. (2013a). The role and mechanism-of-action of Sema3E and Plexin-D1 in vascular and neural development. Semin Cell Dev Biol *24*, 156–162.

Oh, W.-J., and Gu, C. (2013b). Establishment of Neurovascular Congruency in the Mouse Whisker System by an Independent Patterning Mechanism. Neuron *80*, 458–469.

Pecho-Vrieseling, E., Sigrist, M., Yoshida, Y., Jessell, T.M., and Arber, S. (2009). Specificity of sensory–motor connections encoded by Sema3e–Plxnd1 recognition. Nature *459*, 842–846.

Penrod, R.D., Kourrich, S., Kearney, E., Thomas, M.J., and Lanier, L.M. (2011). An embryonic culture system for the investigation of striatal medium spiny neuron dendritic spine development and plasticity. J Neurosci Meth *200*, 1–13.

Percipalle, P., and Visa, N. (2006). Molecular functions of nuclear actin in transcription. J Cell Biology *172*, 967–971.

Poliak, S., Morales, D., Croteau, L.-P., Krawchuk, D., Palmesino, E., Morton, S., Cloutier, J.-F., Charron, F., Dalva, M.B., Ackerman, S.L., et al. (2015). Synergistic integration of Netrin and ephrin axon guidance signals by spinal motor neurons. Elife *4*, e10841.

Saarikangas, J., Kourdougli, N., Senju, Y., Chazal, G., Segerstråle, M., Minkeviciene, R., Kuurne, J., Mattila, P.K., Garrett, L., Hölter, S.M., et al. (2015). MIM-Induced Membrane Bending Promotes Dendritic Spine Initiation. Dev Cell *33*, 644–659.

Sakurai, A., Jian, X., Lee, C.J., Manavski, Y., Chavakis, E., Donaldson, J., Randazzo, P.A., and Gutkind, J.S. (2011). Phosphatidylinositol-4-phosphate 5-Kinase and GEP100/Brag2 Protein Mediate Antiangiogenic Signaling by Semaphorin 3E-Plexin-D1 through Arf6 Protein*. J Biol Chem *286*, 34335–34345.

Samarakoon, R., Goppelt-Struebe, M., and Higgins, P.J. (2010). Linking cell structure to gene regulation: Signaling events and expression controls on the model genes PAI-1 and CTGF. Cell Signal *22*, 1413–1419.

727 Surmeier, D.J., Ding, J., Day, M., Wang, Z., and Shen, W. (2007). D1 and D2 dopamine-receptor modulation of
728 striatal glutamatergic signaling in striatal medium spiny neurons. Trends Neurosci 30, 228–235.

729 Tata, A., Stoppel, D.C., Hong, S., Ben-Zvi, A., Xie, T., and Gu, C. (2014). An image-based RNAi screen
730 identifies SH3BP1 as a key effector of Semaphorin 3E–PlexinD1 signaling. J Cell Biology 205, 573–590.

731 Tessier-Lavigne, M., and Goodman, C.S. (1996). The Molecular Biology of Axon Guidance. Science 274,
732 1123–1133.

733 Vitriol, E.A., and Zheng, J.Q. (2012). Growth Cone Travel in Space and Time: the Cellular Ensemble of
734 Cytoskeleton, Adhesion, and Membrane. Neuron 73, 1068–1081.

735 Winckler, B., and Mellman, I. (2010). Trafficking Guidance Receptors. Csh Perspect Biol 2, a001826.

736 Yeh, M.L., Gonda, Y., Mommersteeg, M.T.M., Barber, M., Ypsilanti, A.R., Hanashima, C., Parnavelas, J.G.,
737 and Andrews, W.D. (2014). Robo1 Modulates Proliferation and Neurogenesis in the Developing Neocortex. J
738 Neurosci 34, 5717–5731.

739 Yu, J., Lin, S., Wang, M., Liang, L., Zou, Z., Zhou, X., Wang, M., Chen, P., and Wang, Y. (2016). Metastasis
740 suppressor 1 regulates neurite outgrowth in primary neuron cultures. Neuroscience 333, 123–131.

741 Zwaag, B.V.D., Hellemons, A.J.C.G.M., Leenders, W.P.J., Burbach, J.P.H., Brunner, H.G., Padberg, G.W., and
742 Bokhoven, H.V. (2002). PLEXIN-D1, a novel plexin family member, is expressed in vascular endothelium and
743 the central nervous system during mouse embryogenesis. Dev Dynam 225, 336–343.

# Figure legends

**Figure 1. Sema3E-Plexin-D1 signaling induces Mtss1 expression in developing striatonigral projecting neurons in a cell-autonomous manner. (A)** RNA sequencing (RNA-seq) analysis of wild-type (WT) (*Plxnd1$^{f/f}$*) and conditional neuronal knockout (cKO) (*Nes-cre;Plxnd1$^{f/f}$*) pups on P5. The box in red indicates the dorsal striatum region from which RNA was isolated. **(B)** Volcano plot of significant differentially expressed genes (DEGs) between WT and cKO. Blue and red circles indicate significantly down- and upregulated genes, respectively, as indicated by fold change greater than 2. **(C-D)** Western blot image showing Mtss1 in the striatum of WT or cKO and quantification. Error bars, the mean ± standard error of the mean (SEM); **P<0.01 by Student's *t* test; Values are averaged from n=5 for WT and n=4 for cKO **(E-F)** Western blot images and quantification of the striatum of WT or *Sema3e$^{-/-}$* mice on P5. mean ± SEM; *P<0.05 by Student's *t test*; values represent the average values obtained for the WT mice, n=7, and *Sema3e$^{-/-}$* mice, n=8. **(G)** The temporal changes in Plexin-D1 and Mtss1 expression in the striatum from E14.5 to adulthood (8-week-old). **(H)** Immunohistochemistry showing Td-Tomato (red) and Mtss1 (green) in the striatum of the *Drd1a- tdT;Plxnd1$^{f/f}$* or *Nes-cre; Drd1a- tdT;Plxnd1$^{f/f}$* mice on P5. The small boxes in the striatum image are presented in the inset images at better resolution. Scale bars, 200 μm (20 μm in the in the insets). **(I)** Mtss1 expression in the striatum of conditional *Plxnd1* cKO mice from E16.5 to P0 and compared to that in WT control. **(J)** Quantification of Mtss1 expression in (I). mean ± SEM; *$P$<0.05, **$P$<0.01 by Student's *t test*; the values represent the average obtained for the WT, n=4, and cKO, n=4 on E16.5, WT, n=3, and cKO, n=3 on E18.5, WT, n=3, and cKO, n=3 on P0. **(K)** Mtss1 expression in MSNs derived from the striatum of WT and *Plxnd1*-cKO mice on P0 and measured on DIV3 and DIV6 in culture. **(L)** Quantification of the blots shown in (K). mean ± SEM; **P<0.01, ***P<0.001 by two-way ANOVA with Tukey's post-hoc corrected for multiple comparison; n=3. n.s., not significant; Str, striatum; Cx, cortex; Th, thalamus; SN, substantia nigra.

768 **Figure 2. The Mtss1 I-BAR domain binds to Plexin-D1 and is Sema3E-independent. (A)** Schematics
769 depicting full-length constructs of Mtss1 and their truncation mutants. **(B)** Coimmunoprecipitation and
770 immunoblot analysis of HEK293T cells transfected with Mtss1-myc with vsv-Plexin-D1. The interaction between
771 Mtss1 and Plexin-D1 was investigated by immunoprecipitation with anti-vsv (top) or anti-myc (bottom) and
772 subsequent western blotting with reciprocal antibodies. **(C)** Immunoprecipitation and western blot analysis after
773 Plexin-D1 and Mtss1 overexpression. Mtss1-myc did not bind to vsv-Plexin-D1ΔICD. **(D)** Identification of the
774 binding domain in Mtss1 that interacts with Plexin-D1 by pull-down and western blot assays. **(E)** Interaction
775 between Mtss1 and Plexin-D1 upon Sema3E (2 nM) treatment.

776

777 **Figure 3. Mtss1 directs Plexin-D1 localization to F-actin-enriched protrusions in COS7 cells. (A)** Cell surface
778 biotinylation and subsequent western blot analysis to analyze surface localization of Plexin-D1 in COS7 cells. **(B)**
779 Quantification of the surface Plexin-D1 level as shown in (A). A.U. indicates arbitrary units. The values represent
780 the averages of the fold ratios compared to those of total Plexin-D1. mean ± SEM; n.s. $P>0.05$ by Student's *t test*;
781 n=3. **(C)** Immunocytochemistry for vsv-Plexin-D1 (red), Mtss1-myc (green), and F-actin (gray) in COS7 cells.
782 Images were obtained by structured illumination microscopy (N-SIM). White arrows (top) indicate colocalized
783 Plexin-D1 and Mtss1 in the protrusion structure. White arrowheads (middle) indicate high Mtss1 levels localized
784 in cell protrusions without Plexin-D1. Yellow arrows (bottom) indicate the normal cell surface with Mtss1ΔI-BAR
785 but no Plexin-D1 colocalization. **(D)** Colocalization rates between vsv signals and myc signals were assessed by
786 Pearson's correlation coefficient. mean ± SEM; *$P<0.05$, **$P<0.01$, ****$P<0.0001$ by one-way ANOVA with
787 Tukey's post-hoc corrected for multiple comparison; vsv-Plexin-D1+Mtss1-myc, n=12; vsv-Plexin-
788 D1ΔICD+Mtss1-myc, n=12; vsv-Plexin-D1+Mtss1ΔI-BAR-myc, n=11. Scale bars, 5 μm.

**Figure 4. Mtss1 places Plexin-D1 in the growth cone to potentiate repulsive signals and contributes to neurite extension. (A)** Immunocytochemistry for vsv-Plexin-D1 (red), Mtss1-myc (green), and F-actin (gray) in the growth cones of MSNs transfected with vsv-Plexin-D1 and Mtss1-myc or Mtss1ΔI-BAR-myc derived from *Mtss1*-null mice. Scale bars, 5 μm. **(B)** Quantification of the intensities in the growth cones. The values represent averages of the fold changes compared to the expression in the control samples (vsv-Plexin-D1+Mtss1-myc). mean ± SEM; ***P*<0.01, ****P*<0.001 by two-way ANOVA with Tukey's post-hoc corrected for multiple comparisons; vsv-Plexin-D1+Mtss1-myc, n=8, and vsv-Plexin-D1+Mtss1ΔI-BAR-myc, n=9. **(C)** Quantification of the colocalization using Pearson's correlation coefficient calculation. mean ± SEM; ***P*<0.01 by Student's *t test*; vsv-Plexin-D1+Mtss1-myc, n=8, and vsv-Plexin-D1+Mtss1ΔI-BAR-myc, n=9. **(D)** A growth cone collapse assay in the presence or absence of Sema3E (2 nM) was performed with MSN cultures derived from WT (*Drd1a-tdT;Mtss1$^{f/f}$*) or cKO (*Drd1a-tdT;Nes-cre;Mtss1$^{f/f}$*) mice. Scale bar, 10 μm. **(E)** Quantification of collapsed growth cones in (D). ***P*<0.01, *****P*<0.0001 by $\chi 2$ test; WT+AP, n=155, WT+AP-Sema3E, n=163, cKO+AP, n=149, cKO+AP-Sema3E, n=149. **(F)** Plexin-D1 expression in the MSNs of *Mtss1*-WT or cKO mice. **(G)** Quantification of Plexin-D1 shown in (F). mean ± SEM; n.s. *P*>0.05 by Student's *t test*; WT n=3, cKO n=4. **(H)** Representative images of Drd1a+ MSNs derived from *Mtss1*-WT or- cKO. Scale bars, 20 μm. **(I)** Quantification of neurite length(Chauvet et al., 2016). The values represent averages of fold changes ratios compared to the length in the control samples (*Mtss1$^{f/f}$* mice treated with AP). mean ± SEM; ***P*<0.01, *****P*<0.0001 by Kruskal-Wallis test with Dunn's post-hoc corrected for multiple comparison; WT+AP, n=179, WT+AP-Sema3E, n=144, cKO+AP, n=184, and cKO+AP-Sema3E, n=147.

**Figure 5. The absence of Mtss1 expression leads to fewer Plexin-D1 molecules localizing to the developing striatonigral projection despite unchanged Plexin-D1 expression in the striatum. (A)** AP-Sema3E binding assay (top) to detect Plexin-D1 expression (white arrows) in striatonigral projections on E17.5 and immunohistochemistry staining (bottom) for neurofilaments (NFs) in adjacent parasagittal sections. The diminished projections are marked by white brackets (middle of the striatum) and arrowheads (near substantia nigra regions). Scale bars, 1 mm (top images) and 500 μm (bottom images). **(B)** Coronal view of Plexin-D1 localization in striatonigral projections. Yellow dotted lines indicate the corridor between the thalamus and globus pallidus. Insets show in the images in dotted boxes at higher resolution. Scale bars, 1 mm (top) and 200 μm (bottom insets). **(C)** Schematic representing the quantified region. The dotted red lines indicate the striatonigral projection-covering areas. The width (blue segment) of the striatonigral tract was measured as previously described(Burk et al., 2017). **(D)** Quantification of the Plexin-D1-positive area in the total striatonigral projection. mean ± SEM; $^{**}P<0.01$ by Student's *t test*; WT, n=12, cKO, n=12 (3 sections/mouse). **(E)** AP-Sema3E binding assay in WT or cKO mice on P0 (top) and P5 (bottom). White arrows indicate the striatonigral projections. Scale bars, 1 mm. **(F-I)** Quantification of the Plexin-D1-positive area and projection width on P0 (F and G) and P5 (H and I) according to the scheme shown in (C). mean ± SEM; $^{*}P<0.05$, $^{***}P<0.001$, $^{****}P<0.0001$ by Mann-Whitney test (F-H) and Student's *t* test (I) n=15 at P0 and n=18 on P5 (3 sections/mouse). **(J)** Western blotting of striatal Plexin-D1 expression on P5. **(K)** Quantification shown in (J). mean ± SEM; n.s. $P>0.05$ by Student's *t* test; WT, n=3, cKO, n=4. EP, entopeduncular nucleus; Gp, globus pallidus.

826 **Figure 6. The absence of Mtss1 reduces the direct-pathway projections, and the projections show an**
827 **irregular pattern. (A)** Immunohistochemistry of coronal sections of striatal projections labeled with td-Tomato
828 endogenously expressed through the *Drd1a* promotor in wild-type (*Drd1a-tdT;Mtss1*$^{f/f}$) or *Mtss1*-deficient mice
829 (*Drd1a-tdT;Nes-cre;Mtss1*$^{f/f}$) on P5. The dotted boxes on the left images are shown in the inset images at higher
830 resolution. Scale bars, 1 mm (left column) and 500 μm (inset images). **(B-C)** Quantification of the intensity (B)
831 and area size (C) of the striatonigral projection in the dotted region in the inset images. mean ± SEM; ***$P$<0.001,
832 ****$P$<0.0001 by Mann-Whitney test (B) and Student's $t$ test (C); n=18 per group (6 sections/ mouse). **(D)**
833 Immunohistochemistry of coronal section images on P30. Scale bars, 1 mm (left column) and 500 μm (inset
834 images). **(E-F)** Quantifications as described for the results obtained on P5. mean ± SEM; ****$P$<0.0001 by Mann-
835 Whitney test (E) and Student's $t$ test (F); n=18 per group (6 sections/mouse). **(G-H)** Representative striatonigral
836 projections in parasagittal sections obtained from *Mtss1*-WT or -cKO mice labeled with Drd1a-tdT on P5 (G) or
837 P30 (H). Dotted boxes indicate the area magnified in the right monochrome images. White arrowheads show
838 misguided striatonigral projections observed on P5. Scale bars, 500 μm (left column) and 200 μm (inset images).
839 **(I)** Diagram depicting the width (red line) of the striatonigral pathway measured as described previously(Burk et
840 al., 2017). **(J-K)** Quantification of the width of the striatonigral projections on P5 (J) and P30 (K). mean ± SEM;
841 **$P$<0.01 by Student's $t$ test; WT, n=3, cKO$^{f}$, n=4 on P5, WT, n=4, and cKO, n=3, on P30. **(L)** Schematic diagram
842 summarizing the results. Hp, hippocampus

**Figure 7. The absence of *Plxnd1* recapitulated the phenotypes observed in the *Mtss1* knockout. (A)** Immunohistochemistry of representative striatonigral projection images labeled with Drd1a-tdT in WT (*Drd1a-tdT*;*Plxnd1*$^{f/f}$) or *Plxnd1* cKO mice (*Drd1a-tdT*;*Nes-cre;Plxnd1*$^{f/f}$) on P5. The dotted boxes in the images are shown in the inset image on the right. Scale bars, 1 mm (left column) and 500 μm (inset images). **(B-C)** Quantification of the intensity (B) and area size (C). mean ± SEM; ****$P$<0.0001, by Student's $t$ test; n=18 per group (6 sections/mouse). **(D)** Coronal section images on P30. Scale bars, 1 mm (left column) and 500 μm (inset images). **(E-F)** Quantification of the intensity (E) and the area size (F) on P30. means ± SEM; ***$P$<0.001 by Mann-Whitney test (E) and Student's $t$ test (F); n=18 per group (6 sections/ mouse). **(G-H)** Representative images showing parasagittal sections of brains from WT or *Plxnd1* cKO mice on P5 (G) or P30 (H). Dotted boxes are magnified in the panels on the right. Scale bars, 1 mm (left column) and 500 μm (inset images). Misguided striatonigral projections on P5 (white arrowheads). **(I)** Model showing striatonigral projection via Sema3E-Plexin-D1-Mtss1 complex.

# Supplemental figure legends

**Supplemental Fig. 1. Identification of Mtss1 in the striatum on P5 through RNA sequencing (RNA-seq) analysis. (A)** Expression of *Plxnd1* mRNA from wild-type (WT) (*Plxnd1*$^{f/f}$) or conditional knockout (cKO) (*Nes-cre;Plxnd1*$^{f/f}$) littermate mouse striatum on P5 was examined via *in situ* hybridization (ISH). Scale bar, 500 μm. **(B)** *Plxnd1* mRNA expression was determined by reverse transcription-polymerase chain reaction (RT–PCR). **(C)** Common gene expression patterns were determined through two independent experiments and by RNA-seq. The values in the principal component analysis (PCA) plot indicate the amount of variation attributed to each principal component. Small circles indicate individual samples, and large ovals represent experimental groups. **(D)** Heatmap showing differential gene expression patterns as determined through RNA-seq analysis. Each row represents hierarchically clustered genes, and each column represents experimental samples with dendrograms and clusters generated with RNA-seq data. Red in the heatmap indicates upregulation of gene expression, and blue denotes downregulation of gene expression; measures were based on z score. **(E)** Most highly enriched Gene Ontology (GO) biological process and cellular component categories in *Nes-cre;Plxnd1*$^{f/f}$ samples were visualized on the basis of significant differentially expressed genes (DEGs) determined by RNA-seq. The size of a circle represents enriched genes, and the color represents $-\log_{10}$ of the P value. Relative levels of *Mtss1* expression in the striatum of *Plxnd1*$^{f/f}$ or *Nes-cre;Plxnd1*$^{f/f}$ mice on P5 were compared by RNA-seq **(F)** and quantitative RT-PCR (qRT-PCR) **(G)** Error bars, the mean ± standard error of the mean (SEM); **P<0.01 by Student's *t* test; *Plxnd1*$^{f/f}$, n=16, *Nes-cre;Plxnd1*$^{f/f}$, n=14, in four independent experiments.

**Supplemental Fig. 2. Selective expression of Mtss1 in the mouse striatum on P5.** Immunohistochemistry staining for *Drd1a* (red) and *Mtss1* (green) in sagittal sections of the striatum and the cortex of the *Drd1a-tdT* mouse brain on P5. Boxed areas are shown in the magnified images. Scale bar, 500 μm (top) and 50 μm (magnified images in the bottom two panels). Cx, cortex, and Str, striatum.

879 **Supplemental Fig. 3. Sema3E expression through thalamostriatal projection on E16.5. (A)** The expression
880 levels of *Plxnd1* mRNA (green) and *Sema3e* mRNA (red) in the brains of E16.5 mice were detected by double
881 fluorescence immunohistochemistry. The red arrow in the bottom right image indicates the Sema3E protein
882 detected by AP-Plexin-D1-ECD (extracellular domain). Scale bar, 1 mm. **(B)** Thalamostriatal projections in the
883 parasagittal sections of the brains on E16.5 were stained by DiI to visualize the projecting axons from neurons in
884 the thalamus. Scale bar, 500 μm. **(C)** Sema3E protein in the striatum of E16.5 brain was detected by western blot
885 analysis. Cx, cortex; Str, striatum; and Th, thalamus.

886

887 **SupplementalFig. 4. Mtss1 expression affects neither Plexin-D1 endocytosis nor Sema3E binding with**
888 **Plexin-D1 but leads to morphological changes of COS7 cells. (A)** Endocytosed biotinylated vsv-PlexinD1 was
889 detected by western blot analysis following cell surface stripping in the presence or absence of AP-Sema3E (2
890 nM). **(B)** Quantification of samples shown in (A). The values in the graph are averages of fold change compared
891 to the expression in control samples (vsv-Plexind1 treated with AP-Sema3E) in three independent experiments.
892 Error bars, the mean ± SEM; n.s. $P>0.05$ by Student's *t* test; in three independent experiments. **(C)** Mtss1 did not
893 affect the interaction between Sema3E and Plexin-D1, as quantified by AP-Sema3E binding assay. The values in
894 the graph represent averages of fold changes compared to the expression in control samples (vsv-Plexind1 treated
895 with AP-Sema3E). Error bars, the mean ± SEM; n.s. $P>0.05$ by Kruskal-Wallis test with Dunn's post-hoc corrected
896 for multiple comparison; vsv-Plexin-D1+AP, n=8; vsv-Plexin-D1+Mtss1-myc+AP, n=7; vsv-Plexin-D1+AP-
897 Sema3E, n=8; and vsv-Plexin-D1+Mtss1-myc+AP-Sema3E, n=8, in three independent experiments. **(D)**
898 Schematics describing the full-length construct of Mtss1-myc and its deletion mutant constructs (Mtss1ΔI-BAR-
899 myc, Mtss1ΔWH2-myc, and I-BAR-myc). **(E)** Immunocytochemistry images taken after overexpression of each
900 construct. Constructs show the I-BAR domain leading to diverse cell protrusion morphologies. Some of the
901 protrusions were excessively spiked (arrows) or thin and long (arrowheads). Overexpression of the I-BAR domain
902 only (I-BAR-myc) can induce extreme protrusion structures. Scale bar, 20 μm.

**Supplemental Fig. 5. The Sema3E-Plexin-D1-Mtss1 signaling axis specifically regulates the neurite extension of direct-pathway MSNs. (A)** Representative images showing Drd1a-tdT-positive MSNs derived from *Drd1a-tdT;Plxnd1$^{f/f}$* or *Drd1a-tdT;Nes-cre;Plxnd1$^{f/f}$* mice in the presence or absence of AP-Sema3E and cultured for 3 days. Scale bars, 20 μm. **(B)** The growth of neurites of Drd1a-tdT-positive MSNs was inhibited by treatment with AP-Sema3E, whereas MSNs lacking *Plxnd1* did not respond to AP-Sema3E treatment. The values in the graph represent averages of fold changes compared to the expression in the control samples (*Plxnd1$^{f/f}$* mice treated with AP). Error bars, the mean ± SEM; ****$P$<0.0001 by Kruskal-Wallis test with Dunn's post-hoc corrected for multiple comparison; *Drd1a-tdT;Plxnd1$^{f/f}$* +AP, n=161; *Drd1a-tdT;Plxnd1$^{f/f}$* +AP-Sema3E, n=145; *Drd1a-tdT;Nes-cre;Plxnd1$^{f/f}$* +AP, n=144; and *Drd1a-tdT;Nes-cre Plxnd1$^{f/f}$* +AP-Sema3E, n=109, in three independent experiments. **(C)** The percentage of Drd1a-positive MSNs with neurites shorter than twice the cell body diameter. *$P$<0.05, **$P$<0.01 by $\chi 2$ test; *Mtss1$^{f/f}$* +AP, n=48; *Mtss1$^{f/f}$* +AP-Sema3E, n=47; *Nes-cre;Mtss1$^{f/f}$* +AP, n=48, *Nes-cre;Mtss1$^{f/f}$* +AP-Sema3E, n=48, in four independent experiments.

**Supplemental Fig. 6. The absence of Mtss1 does not affect MSN survival or dendritic arborization during striatonigral pathway development. (A)** Immunohistochemistry staining for cleaved caspase 3 (CC3), marked by white arrowheads in the striatum of wild-type (WT) (*Mtss1$^{f/f}$*) or conditional knockout (cKO) (*Nes-cre;Mtss1$^{f/f}$*) mice. Scale bar, 200 μm. **(B)** Cell death was quantified by the number of CC3-positive cells in a 1x1 mm$^2$ area covering the dorsal part of the striatum in *Mtss1$^{f/f}$* or *Nes-cre;Mtss1$^{f/f}$* mice. Error bars, the mean ± SEM; n.s. $P$>0.05 by Mann-Whitney test; *Mtss1$^{f/f}$*, n=20; *Nes-cre;Mtss1$^{f/f}$*, n=20 (5 sections/ mouse). **(C)** Representative Golgi staining images at low (top panels) and high magnification (bottom panels). Scale bar, 100 μm. **(D)** Sholl analysis of dendritic morphology. The number of dendritic intersections on concentric rings spaced at 10 μm intervals from the soma. No difference was found between WT and cKO mice. Error bars, the mean ± SEM; n.s. $P$>0.05 by two-way ANOVA with Bonferroni's post-hoc corrected for multiple comparison; *Mtss1$^{f/f}$*, n =12; *Nes-cre;Mtss1$^{f/f}$*, n=15, of 3 mice. **(E)** Dendrite length analysis was performed with ImageJ. Error bars, the means ± SEM; n.s. $P$>0.05 by Student's $t$ test; *Mtss1$^{f/f}$*, n =12, and *Nes-cre;Mtss1$^{f/f}$*, n=15, from 3 mice.

**Supplemental Fig. 7. Schematic summary showing striatonigral projection development via a serial reciprocal interaction of Sema3E-Plexin-D1-Mtss1 complex.**

# Figure 1

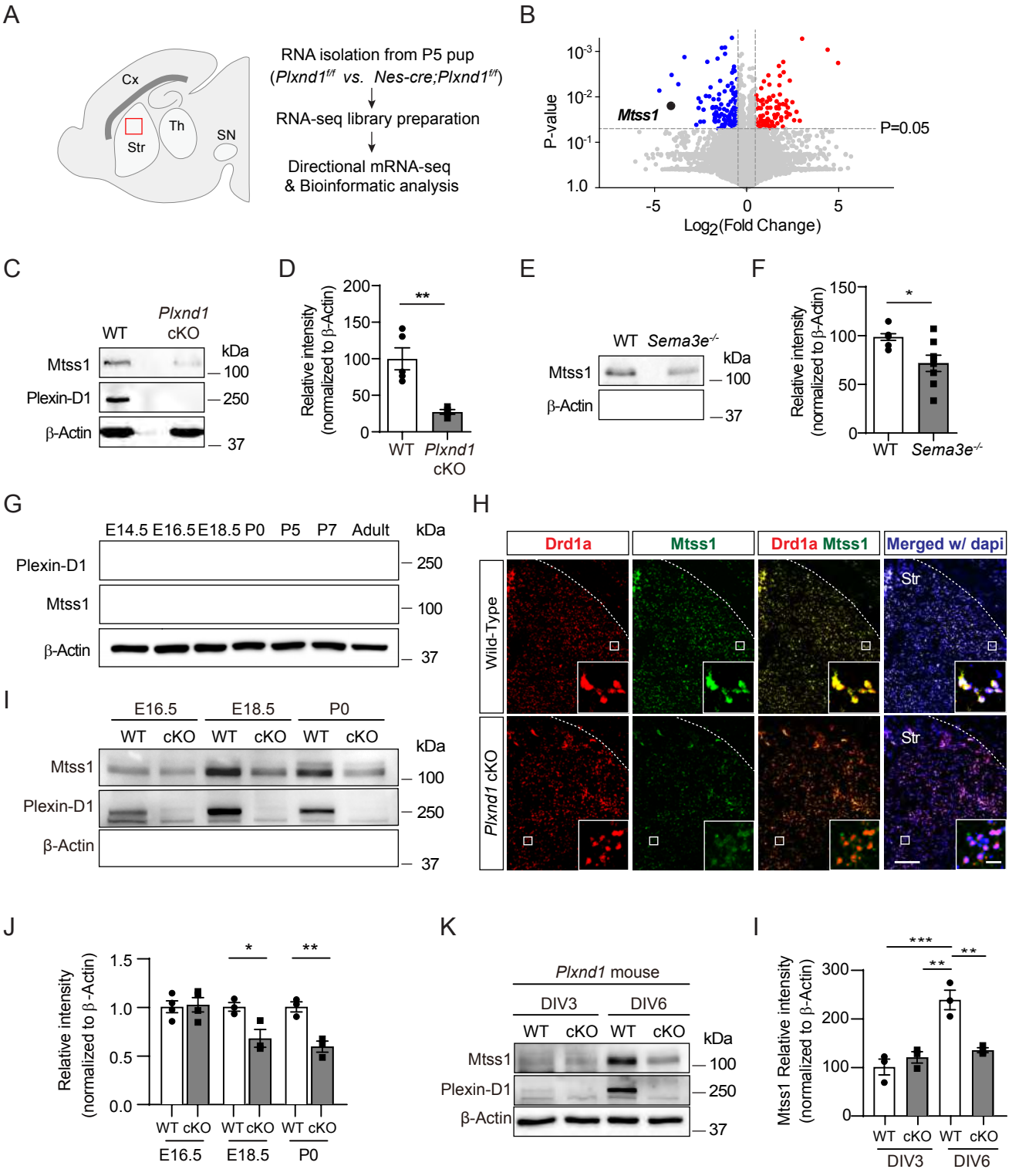

# Figure 2

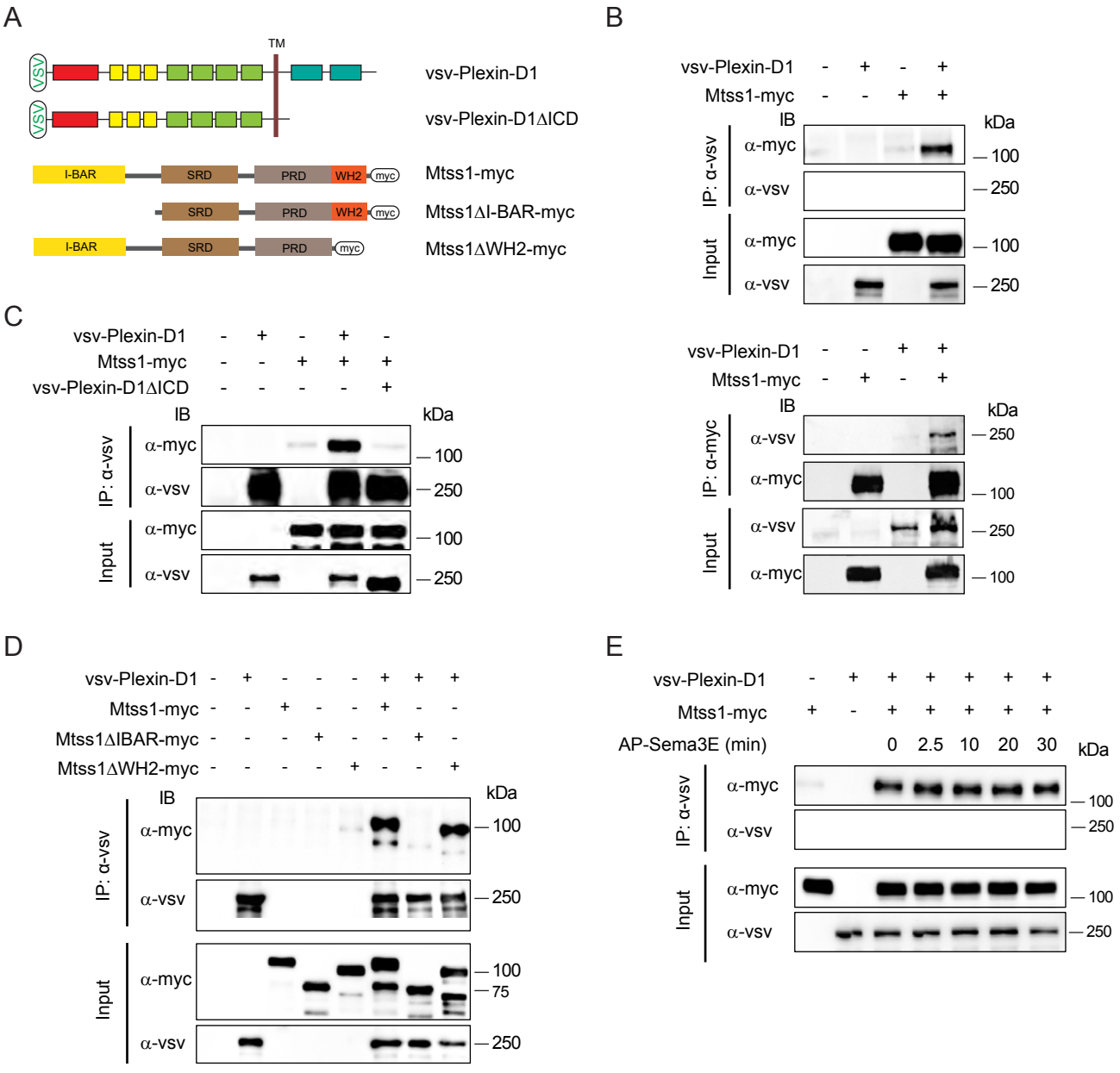

# Figure 3

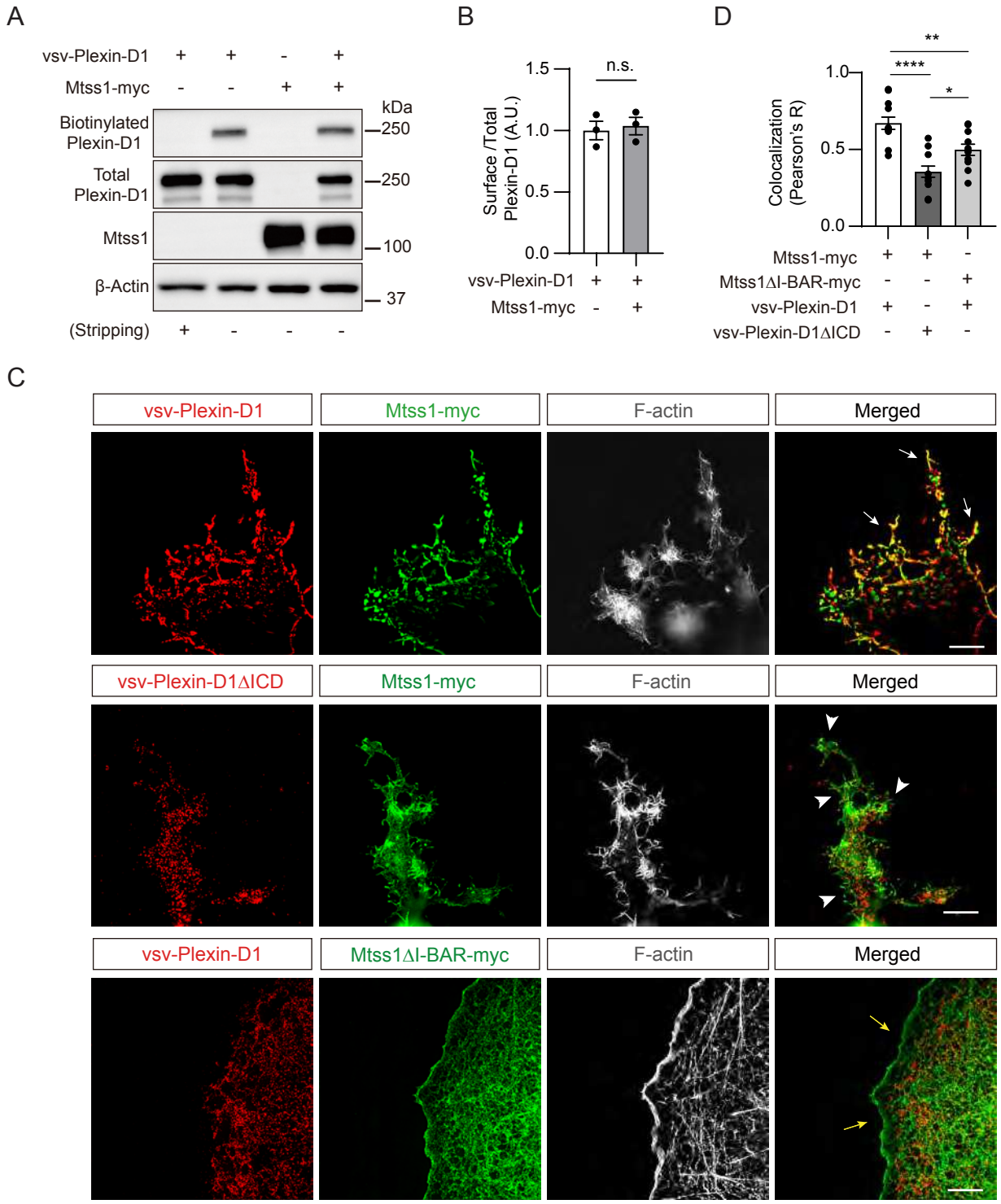

# Figure 4

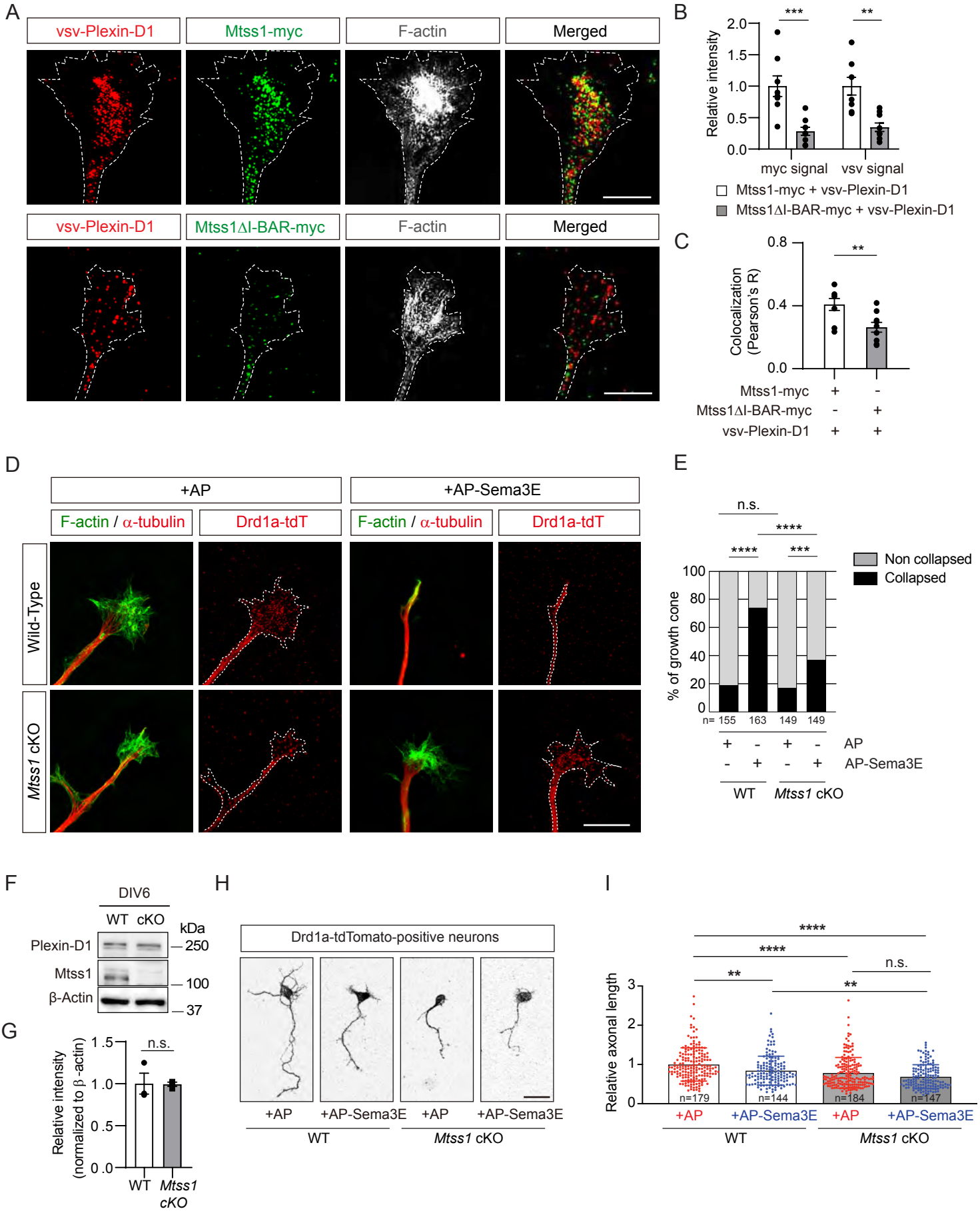

# Figure 5

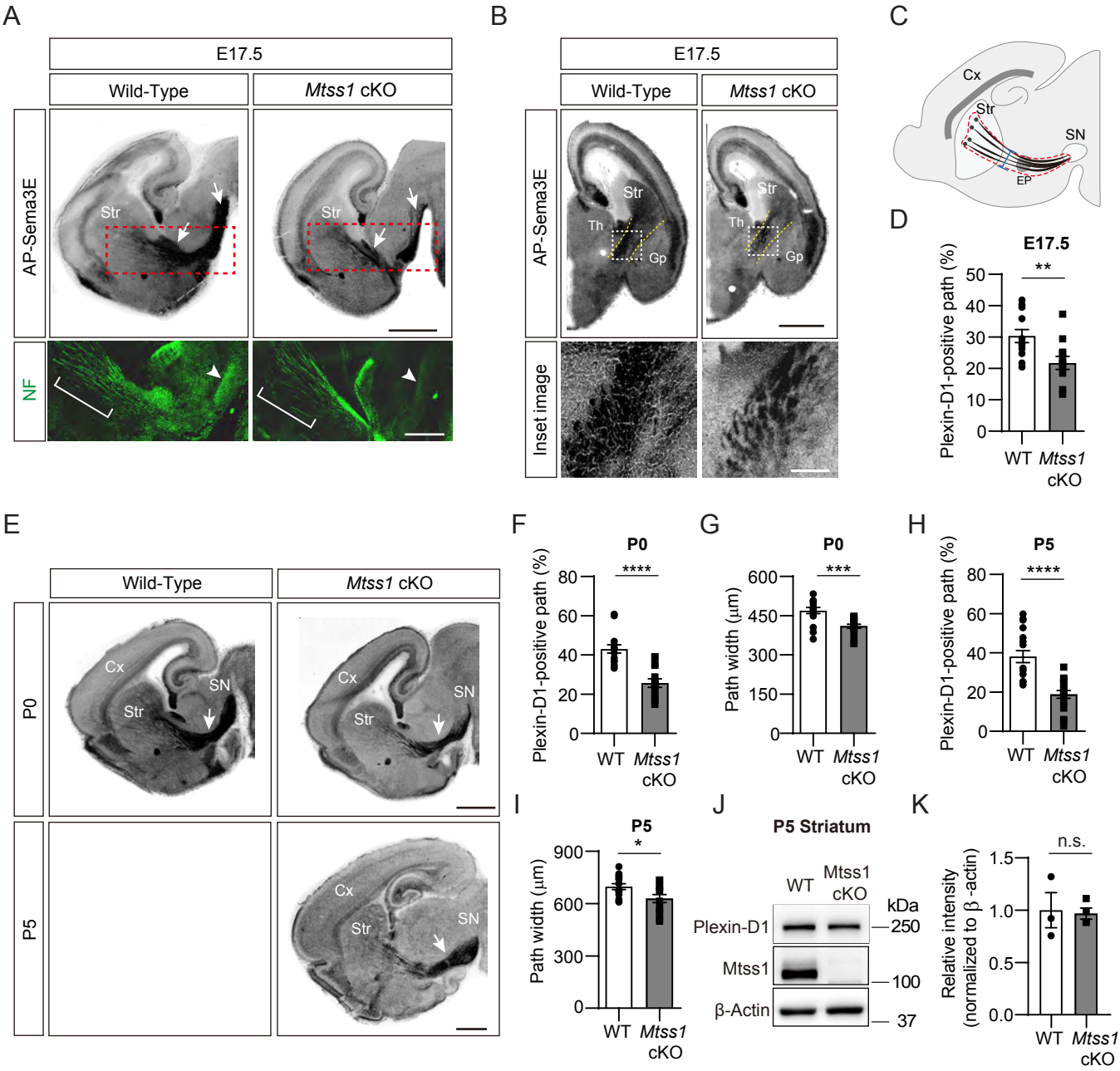

# Figure 6

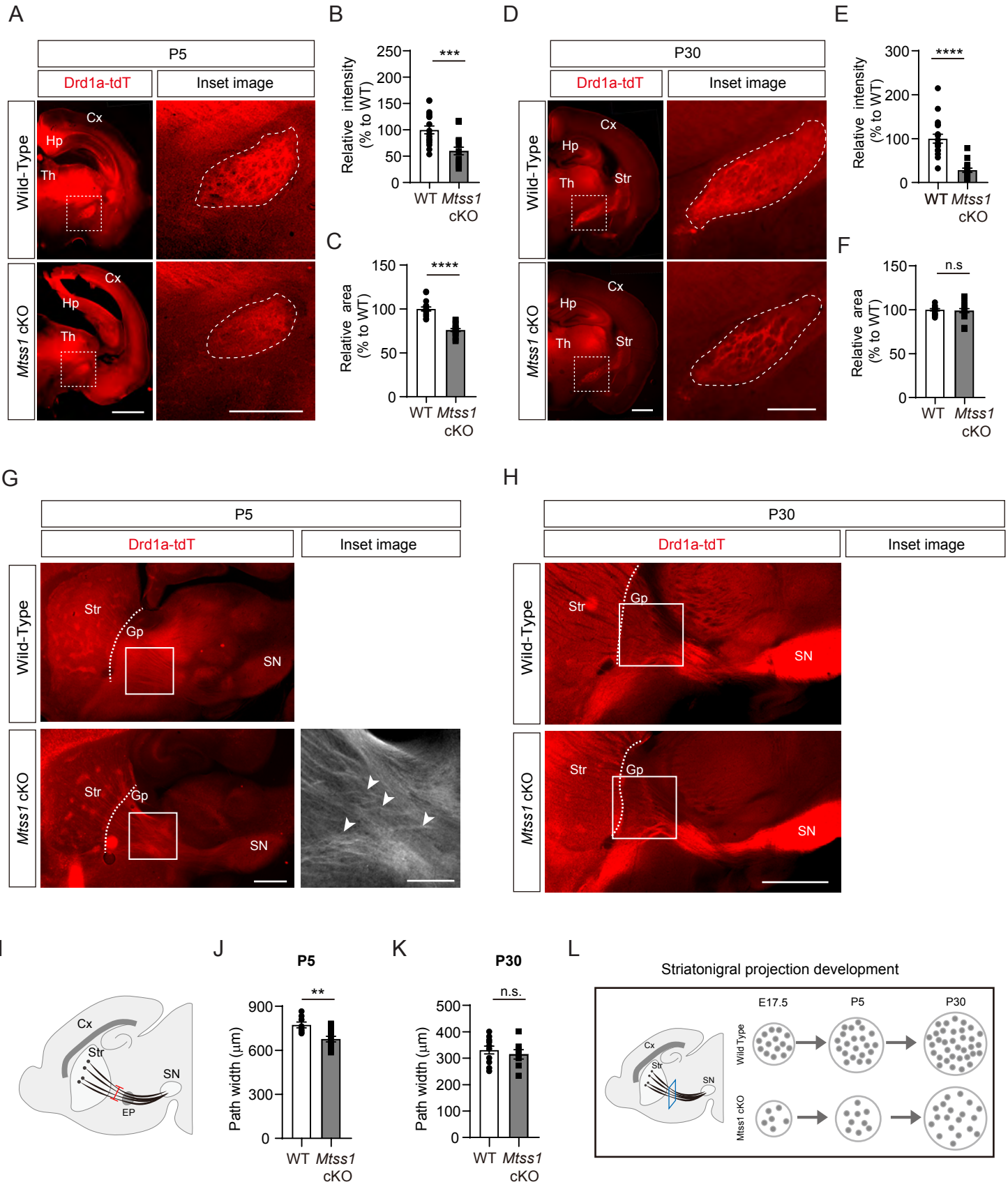

# Figure 7

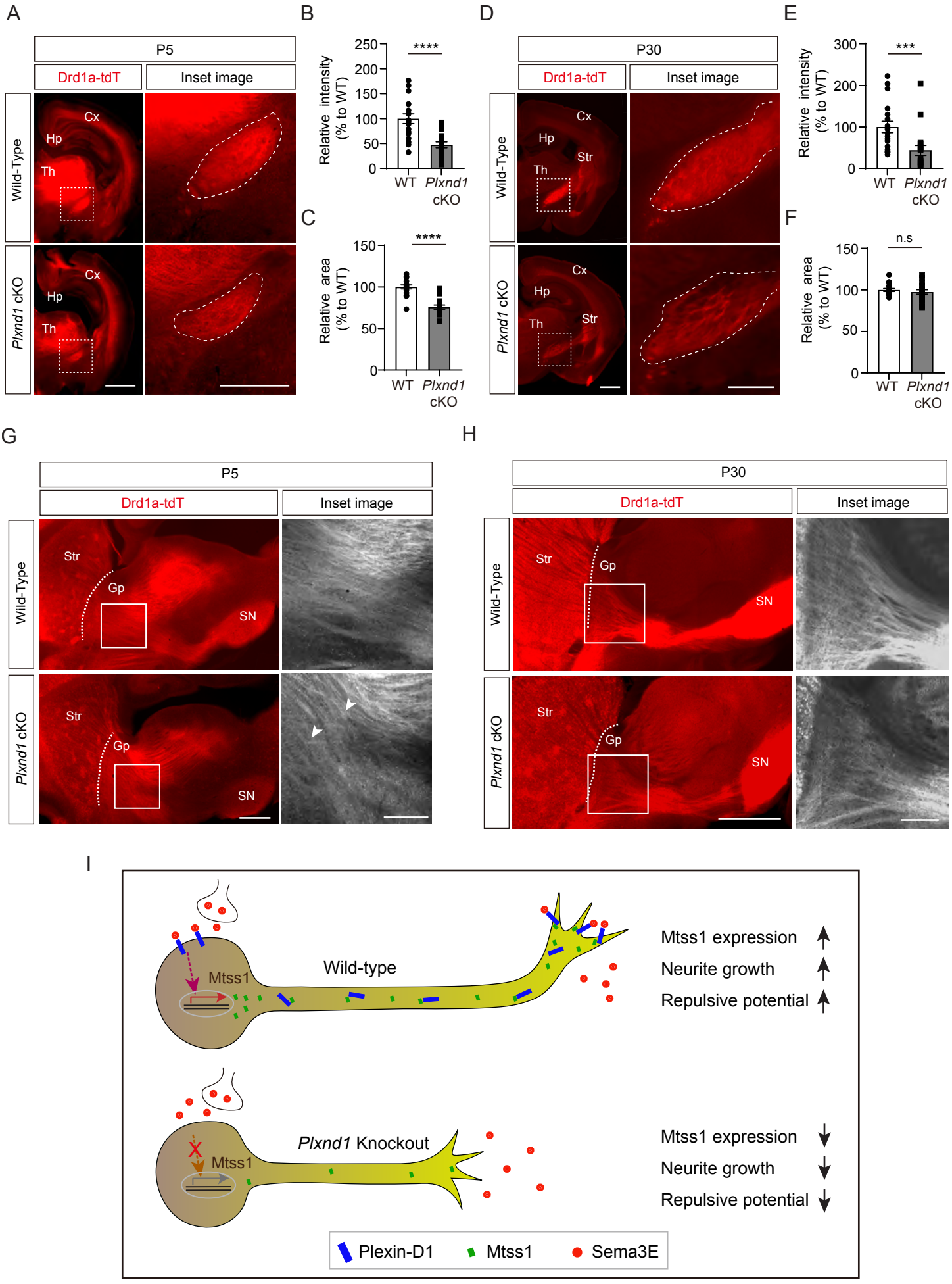

# Supplementary Figure 1

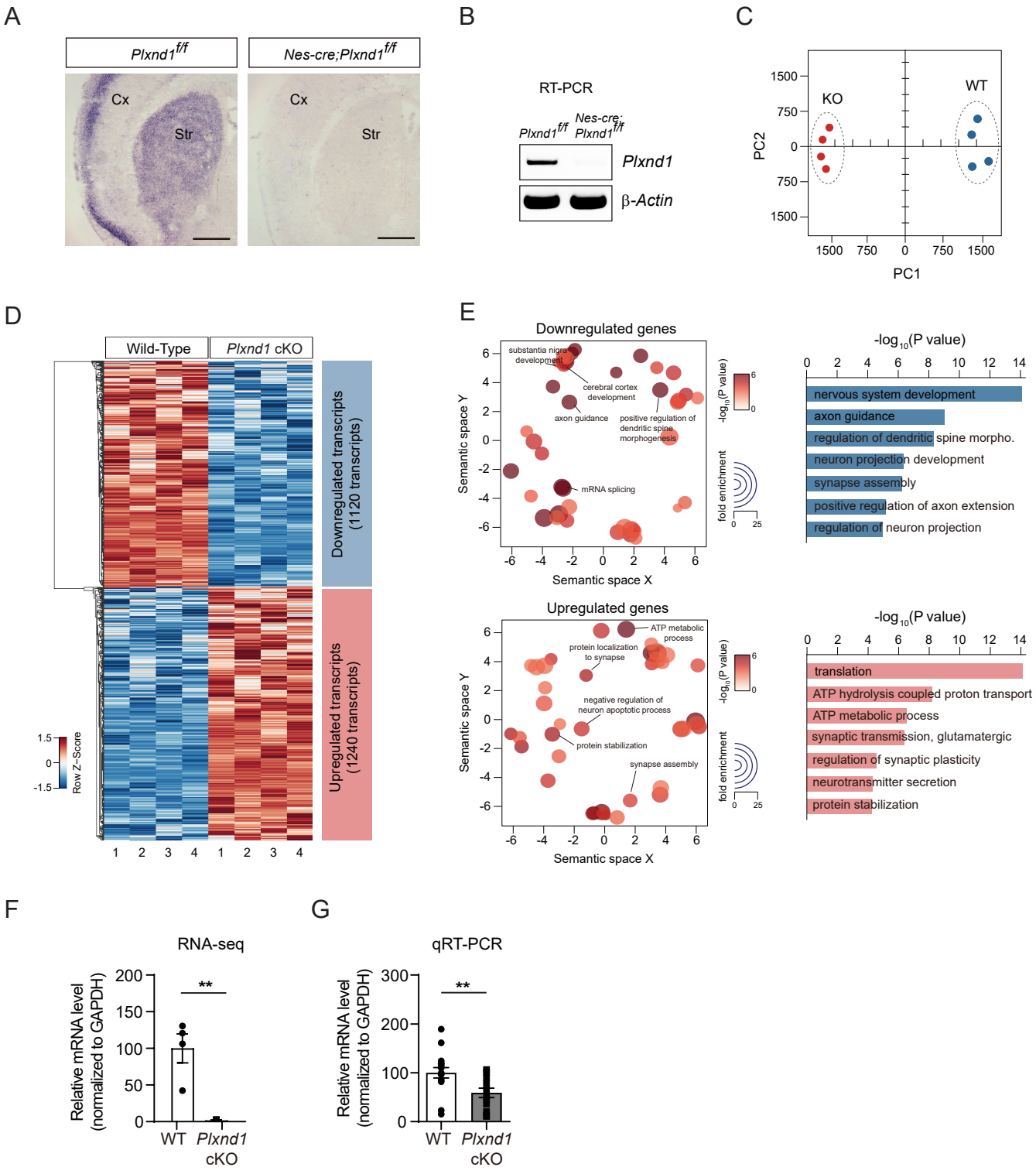

# Supplementary Figure 2

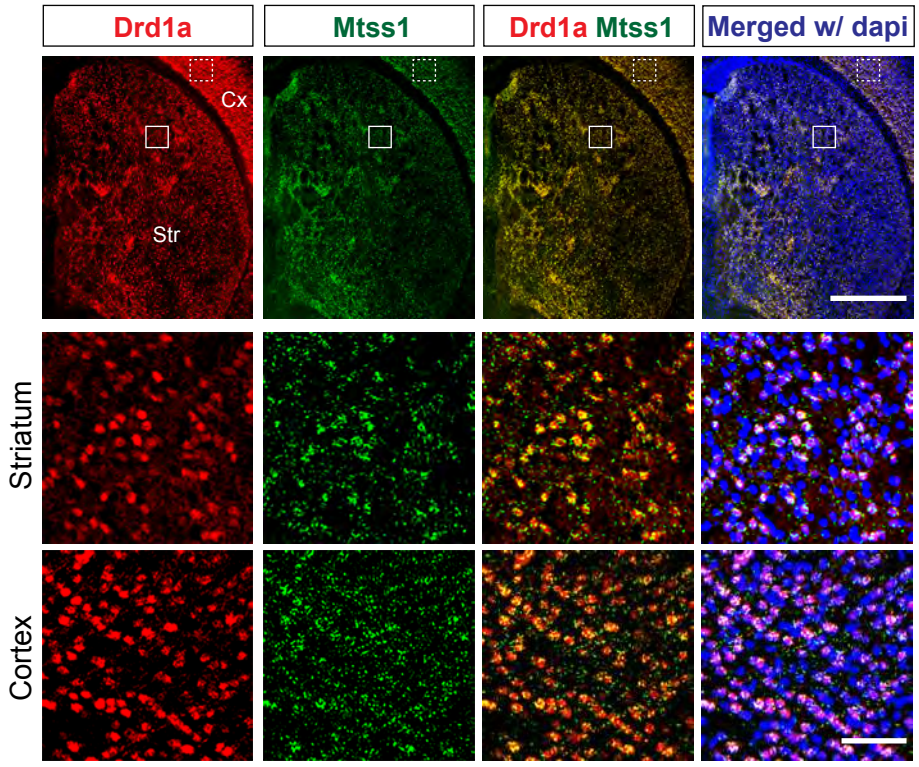

# Supplementary Figure 3

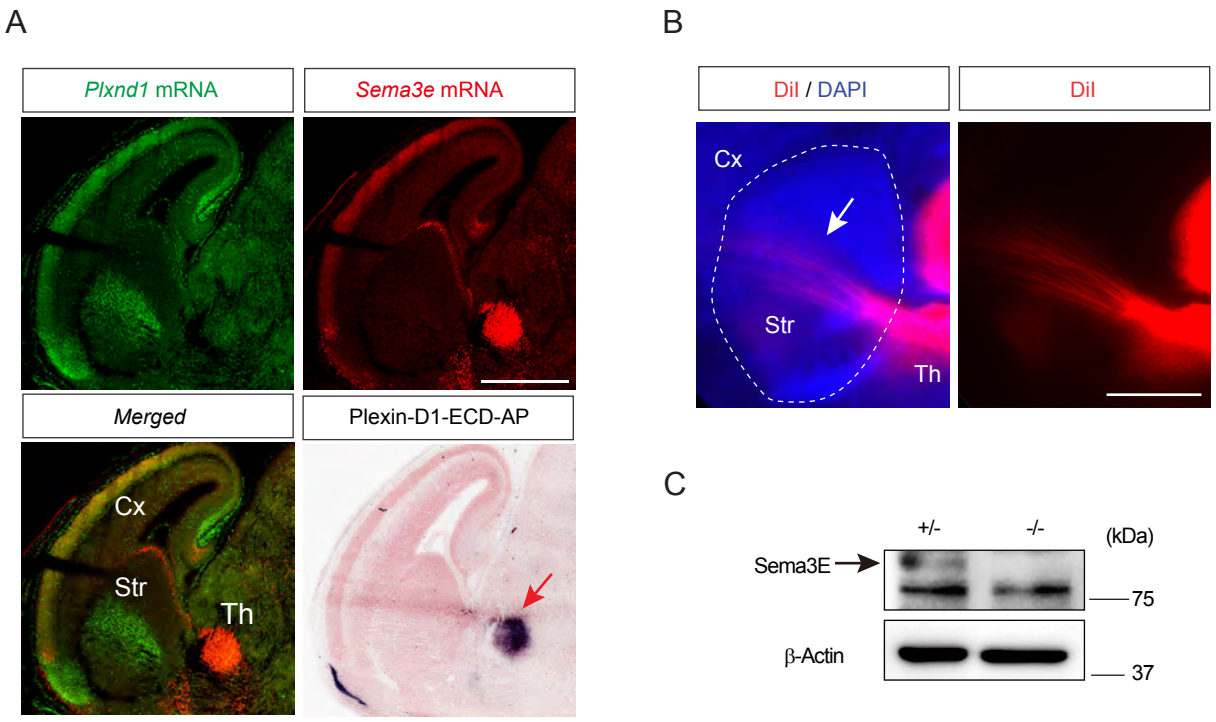

# Supplementary Figure 4

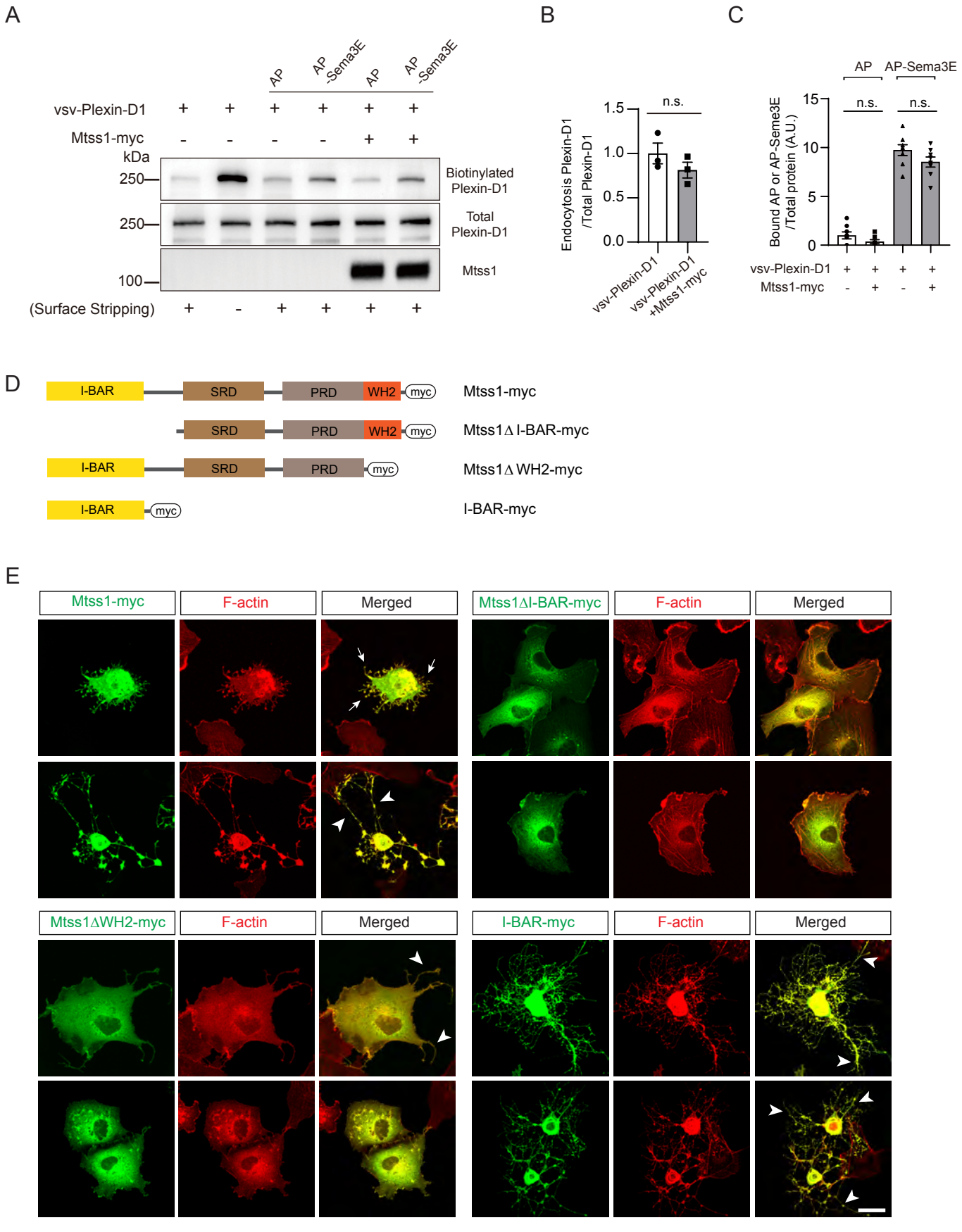

# Supplementary Figure 5

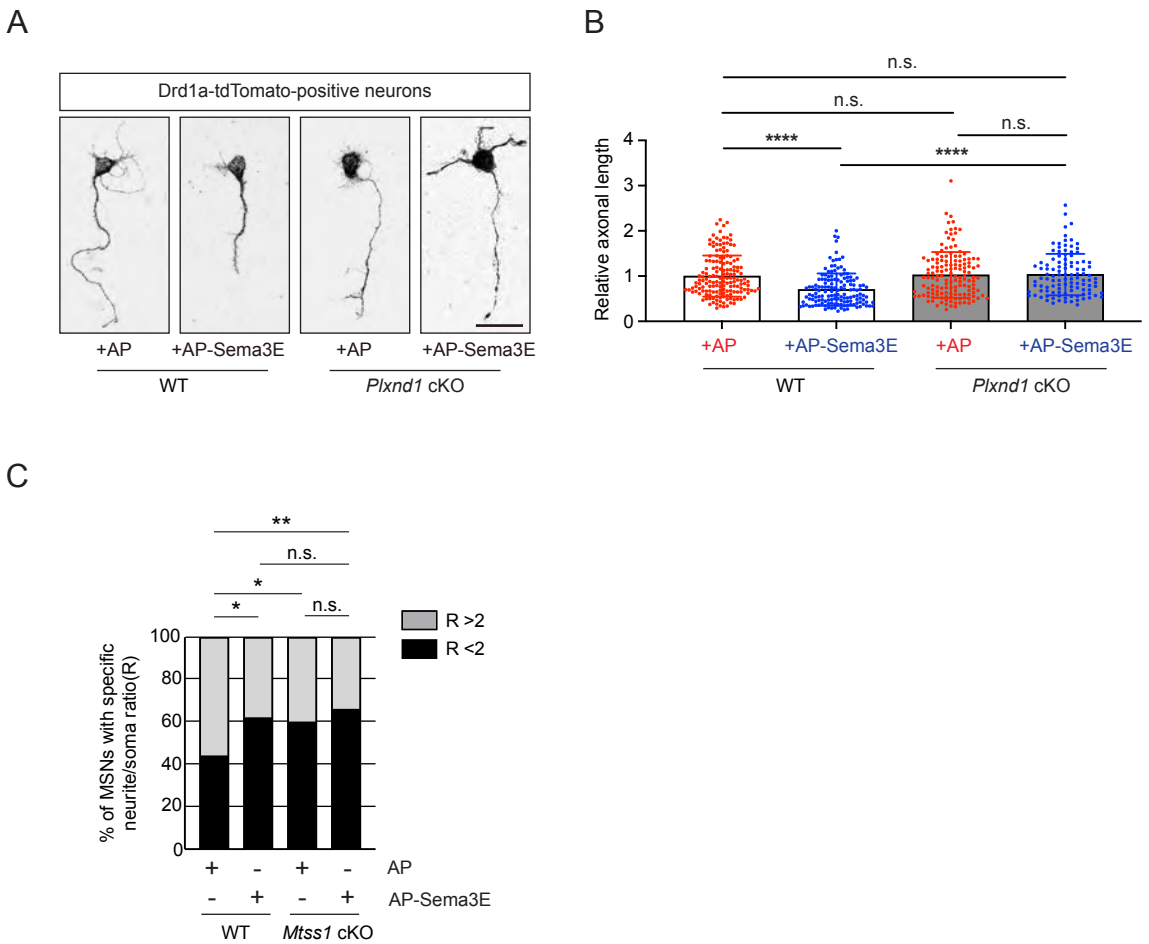

# Supplementary Figure 6

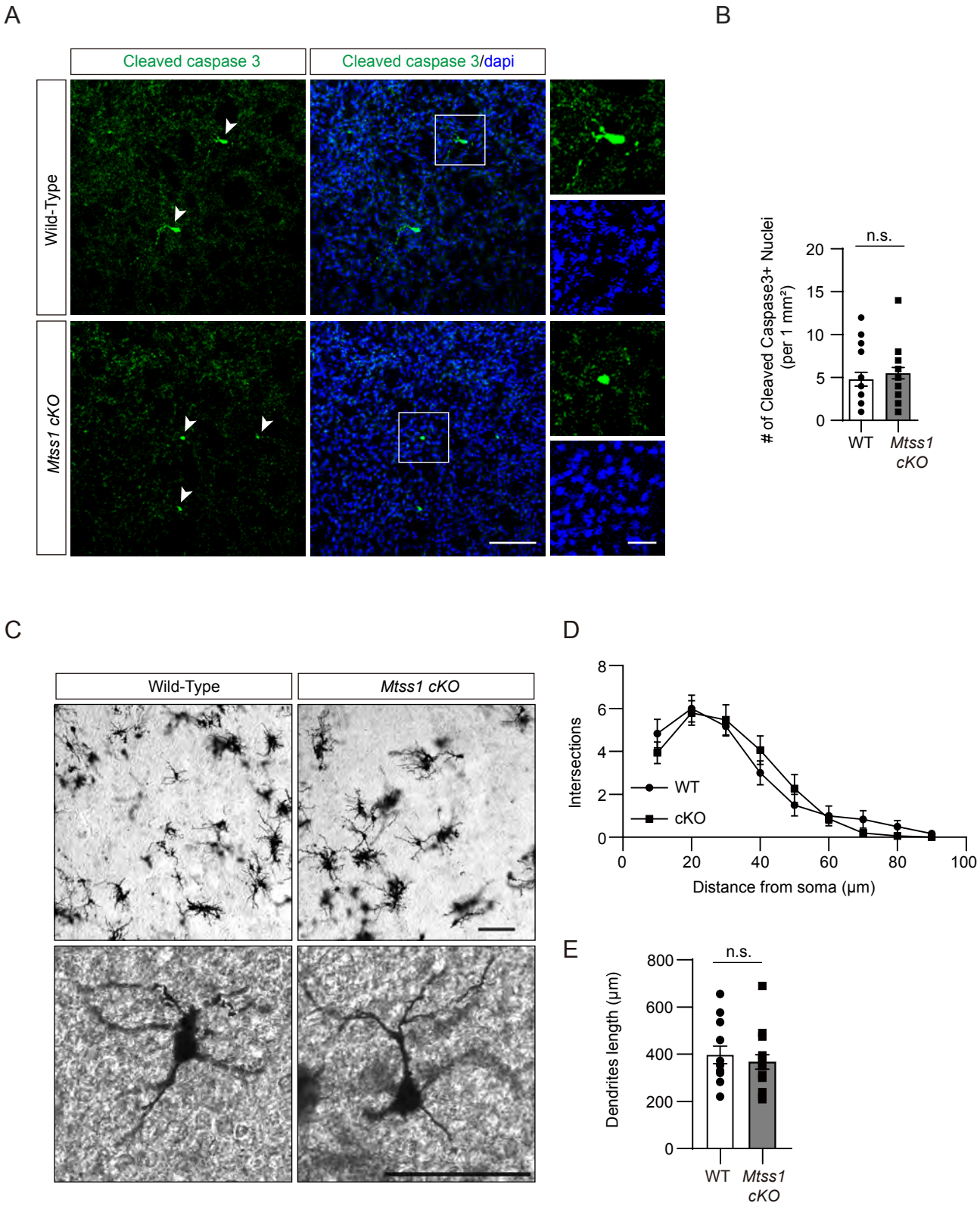

# Supplementary Figure 7

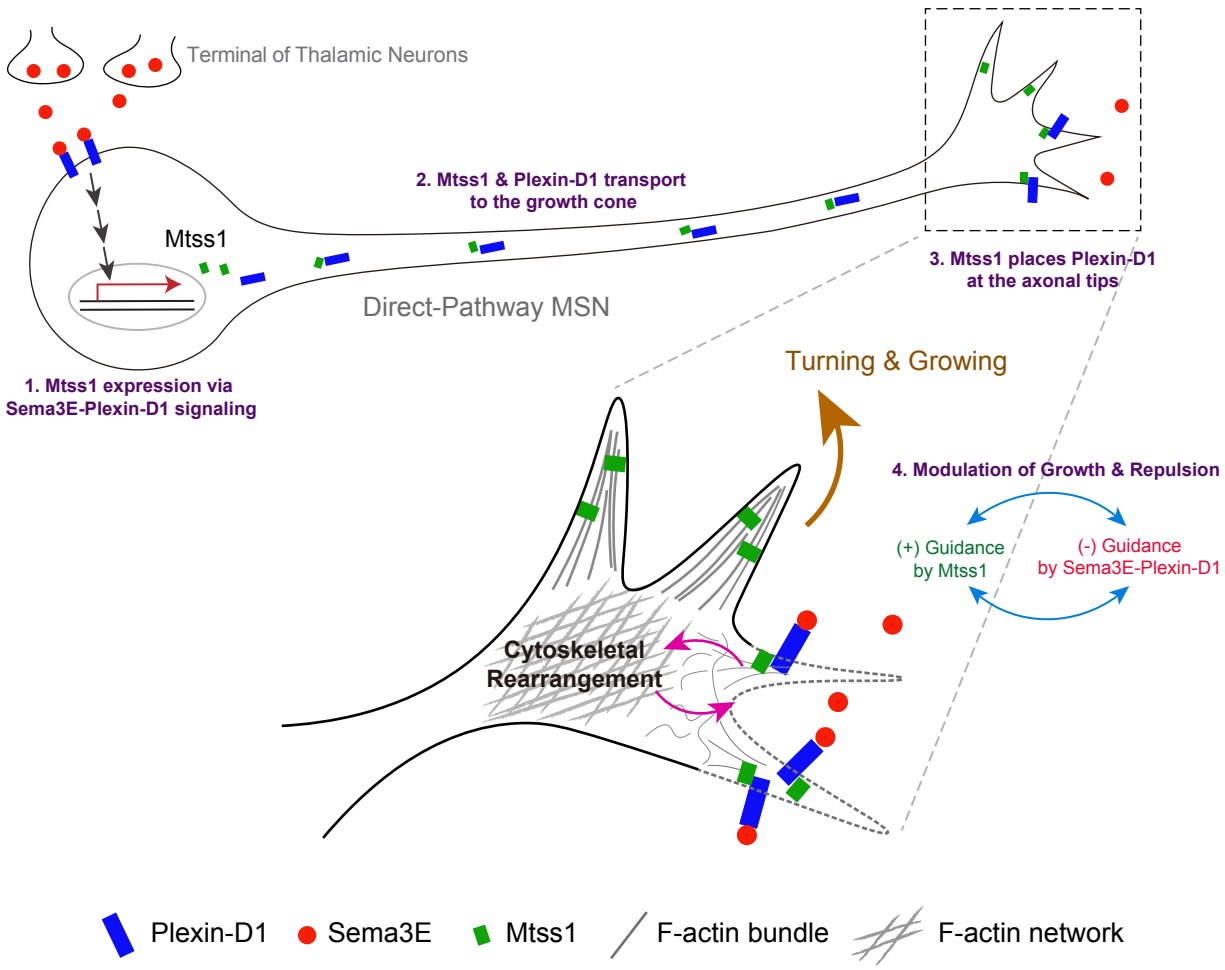

# Supplementary Table 1

**KEY RESOUCES TABLE**

| REAGENT or RESOURCE | SOURCE | IDNETIFIER |
|---|---|---|
| **Antibodies** | | |
| Rabbit anti-Mtss1 | Novus Biologicals | Cat# NBP2-24716<br>RRID: AB_2716709 |
| Goat anti-Plexin-D1 | R&D systems | Cat# AF4160<br>RRID: AB_2237261 |
| Rabbit anti-β-actin/HRP | Cell Signaling Technology | Cat# 5125S<br>RRID:AB_1903890 |
| Mouse anti-Myc | Cell Signaling Technology | Cat# 2276<br>RRID:AB_331783 |
| Goat anti-Vsv | Abcam | Cat# ab3861<br>RRID:AB_304118 |
| Human anti-Sema3E | LSBio | Cat# LS-c353198 |
| Rabbit anti-RFP | Abcam | Cat# ab62341<br>RRID:AB_945213 |
| Mouse anti-RFP | Thermo Fisher Scientific | Cat# MA5-15257<br>RRID:AB_10999796 |
| Mouse anti-alpha-tubulin | Sigma-Aldrich | Cat# T5168<br>RRID:AB_477579 |
| Rabbit anti-cleaved caspase3 | Cell Signaling Technology | Cat# 9661<br>RRID:AB_2341188 |
| anti-digoxigenin-alkaline phosphatase | Roche | Cat# 11093274910<br>RRID:AB_2313640 |
| Goat anti-mouse IgG/HRP | Thermo Fisher Scientific | Cat# 31430<br>RRID:AB_228307 |
| Donkey anti-rabbit IgG/HRP | Jackson ImmunoReasearch | Cat# 711-035-152<br>RRID:AB_10015282 |

| | | |
|---|---|---|
| Donkey anti-goat IgG/HRP | Jackson ImmunoReasearch | Cat# 705-035-147<br>RRID:AB_2313587 |
| Donkey anti-rabbit IgG, Alexa Fluor 488 | Thermo Fisher Scientific | Cat# A-21206<br>RRID:AB_2535792 |
| Donkey anti-mouse IgG, Alexa Fluor 488 | Thermo Fisher Scientific | Cat# A-21202<br>RRID:AB_141607 |
| Donkey anti-goat IgG, Alexa Fluor 568 | Thermo Fisher Scientific | Cat# A-11057<br>RRID:AB_142581 |
| Donkey anti-rabbit IgG, Alexa Fluor 568 | Thermo Fisher Scientific | Cat# A-10042<br>RRID:AB_2534017 |
| Donkey anti-mouse IgG, Alexa Fluor 568 | Thermo Fisher Scientific | Cat# A-10037<br>RRID:AB_2757558 |
| Donkey anti-mouse IgG, Alexa Fluor 647 | Thermo Fisher Scientific | Cat# A-31571<br>RRID:AB_162542 |
| | | |
| | | |
| | | |
| Chemicals, peptides, and kits | | |
| TRIzol™ Reagent | Thermo Fisher Scientific | Cat# 15596026 |
| QuantiTect Reverse Transcription kit | Qiagen | Cat# 205313 |
| LightCycler 480 SYBR Green I Master | Roche | Cat# 04 887 352 001 |
| RNasin® Ribonuclease Inhibitor | Promega | Cat# N2115 |
| Halt™ Protease and Phosphatase Inhibitor Cocktail | Thermo Fisher Scientific | Cat# 78444 |
| Pierce™ BCA Protein Assay Kit | Thermo Fisher Scientific | Cat# 23225 |
| Immobilon-P PVDF Membrane | Merck | Cat# IPVH00010 |
| SuperSignal™ West Pico PLUS Chemiluminescent Substrate | Thermo Fisher Scientific | Cat# 34580 |
| SuperSignal™ West Femto Maximum Sensitivity Substrate | Thermo Fisher Scientific | Cat# 34096 |

| | | |
|---|---|---|
| ProLong™ Diamond Antifade Mountant with DAPI | Thermo Fisher Scientific | Cat# P36962 |
| Eukitt® Quick-hardening mounting medium | Sigma-Aldrich | Cat# 03989 |
| Alexa Fluor™ 488 Phalloidin | Thermo Fisher Scientific | Cat# A12379 |
| Alexa Fluor™ 568 Phalloidin | Thermo Fisher Scientific | Cat# A12380 |
| Alexa Fluor™ 647 Phalloidin | Thermo Fisher Scientific | Cat# A22287 |
| Gibco™ DMEM, high glucose, pyruvate | Gibco™ | Cat# 11995-065 |
| Fetal Bovine Serum | Hyclone | Cat# SH30084.03 |
| Penicillin-Streptomycin | HyClone | Cat# SV30010 |
| Opti-MEM™ I Reduced Serum Medium | Gibco™ | Cat# 31985070 |
| HyClone Dulbecco's Phosphate Buffered Saline | HyClone | Cat# SH30028.02 |
| HBSS, no calcium, no magnesium | Gibco™ | Cat# 14170120 |
| Paraformaldehyde | Electron Microscopy Sciences | Cat#19202 |
| Magnesium chloride | Sigma-Aldrich | Cat# M8266 |
| Poly-D-lysine hydrobromide | Sigma-Aldrich | Cat# P6407 |
| Corning® Laminin | Corning | Cat# 354232 |
| Lipofectamine™ 2000 Transfection Reagent | Thermo Fisher Scientific | Cat# 11668019 |
| Basic NucleofectorTM Kit | LONZA | Cat# VAPI-1003 |
| NBT/BCIP Ready-to-Use Tablets | Roche | Cat# 11697471001 |
| DiI (1.1-dioctadecyl-3,3,3,3-tetramethyl-indocarbocyanine perchlorate) | Sigma-Aldrich | Cat# 468495 |
| FD Rapid GolgiStain™ Kit | FD neurotechnologies Inc. | Cat# PK401A |
| | | |
| Deposited data | | |
| RNA-seq (P5 mice, striatum) | This paper | GEO: GSE196558 |
| | | |

| Experimental models: Organisms/strains | | |
|---|---|---|
| Mouse: C57BL/6J | The Jackson Laboratory | Stock# 000664 |
| Mouse: Nestin-Cre | The Jackson Laboratory | Stock# 003771 |
| Mouse: Drd1a-tdTomato | The Jackson Laboratory | Stock# 016204 |
| Mouse: *Mtss1*$^{flox/+}$ | Center for Animal Resources and Development Database (CARD) under permission of Dr. Mineko Kengaku | Card ID#2760 |
| Mouse: *Plxnd1*$^{flox/flox}$ | Obtained from Dr. Chenghua Gu | Kim et al., 2011 |
| Mouse: *Sema3e*$^{+/-}$ | Obtained from Dr. Chenghua Gu | Chauvet et al., 2007 |
| | | |
| **Software and algorithms** | | |
| Image J | NIH | https://imagej.nih.gov/ij/ |
| Prism 9 | GraphPad | https://www.graphpad.com/scientific-software/prism/ |
| Image Lab (v5.2.1) | BIO-RAD | https://www.bio-rad.com/ |
| Fusion FX | Vilber | https://www.vilber.com/fusion-fx/ |
| LightCycler®480 (v1.5.1) | Roche | https://lifescience.roche.com/ |
| Leica Application Suite X | Leica | https://www.leica-microsystems.com/ |
| NIS-Elements AR (v4.51.00) | Nickon | https://www.microscope.healthcare.nikon.com/ |
| NIS-Elements (v4.50.00) | Nickon | https://www.microscope.healthcare.nikon.com/ |